

Article

Multifunctional Materials Based on the Solid Solutions of the (Na, K, Cd_{0.5})NbO₃ (KNN-Cd) System Modified with Rare Earth Elements: Crystal Structure, Microstructure, and Macroresponses

Andryushin Konstantin ¹, Mikhail Palatnikov ², Lidiya Shilkina ¹, Alexandr Nagaenko ³, Olga Shcherbina ^{2,*}, Maxim Smirnov ², Nikolay Sidorov ², Stanislav Kubrin ¹, Anzhela Rudskaya ⁴, Daniil Rudskiy ¹ and Larisa Reznichenko ¹

¹ Research Institute of Physics, Southern Federal University, Rostov-on-Don 344002, Russia

² Tananaev Institute of Chemistry—Subdivision of the Federal Research Centre, Kola Science Centre of the Russian Academy of Sciences, Apatity 184209, Russia

³ Institute of High Technology and Piezo Technic, Southern Federal University, Rostov-on-Don 344002, Russia

⁴ Faculty of Physics, Southern Federal University, Rostov-on-Don 344002, Russia

* Correspondence: o.shcherbina@ksc.ru

Abstract: Ceramic samples of polycomponent solid solutions (SSs) Na_{0.90}K_{0.05}Cd_{0.05}NbO₃ (Cd-modified KNN) and [(Na_{0.90}K_{0.05}Cd_{0.05})_{0.95}REE_{0.05}]NbO₃, where REE = La, Pr, Tb, Dy, Ho, were obtained by the uniaxial hot pressing (UHP) method. The crystal lattice structures, morphological features of the microstructure, and dielectric and thermophysical properties of these ceramics have been investigated. For the first time, their strength characteristics (Young's modulus) and the critical stress intensity factor of the mode I K_{Ic} have been estimated. Photoluminescent properties have been compared in SSs [(Na_{0.90}K_{0.05}Cd_{0.05})_{0.95}REE_{0.05}]NbO₃ in the visible wavelength range.

Keywords: solid solutions; perovskite; uniaxial hot pressing; microstructure; dielectric and thermophysical properties; microhardness; Young's modulus; crack resistance; luminescence



Citation: Konstantin, A.; Palatnikov, M.; Shilkina, L.; Nagaenko, A.; Shcherbina, O.; Smirnov, M.; Sidorov, N.; Kubrin, S.; Rudskaya, A.; Rudskiy, D.; et al. Multifunctional Materials Based on the Solid Solutions of the (Na, K, Cd_{0.5})NbO₃ (KNN-Cd) System Modified with Rare Earth Elements: Crystal Structure, Microstructure, and Macroresponses. *Ceramics* **2023**, *6*, 342–363. <https://doi.org/10.3390/ceramics6010021>

Academic Editor: Maurizio Ferrari

Received: 27 December 2022

Revised: 27 January 2023

Accepted: 29 January 2023

Published: 1 February 2023



Copyright: © 2023 by the authors. Licensee MDPI, Basel, Switzerland. This article is an open access article distributed under the terms and conditions of the Creative Commons Attribution (CC BY) license (<https://creativecommons.org/licenses/by/4.0/>).

1. Introduction

Almost every decade, starting from the 1950s, marks a new vector of development in functional materials science. Ferroelectricity was discovered in BaTiO₃ in the 1950s, and the materials based on it appeared [1–4]. Compositions based on the binary PZT-system of (Pb(Zr,Ti)O₃) were studied in the 1960s [5,6], including the modified ones [7–10]. Ternary systems of the solid solutions (SS) [11,12] were the most popular materials studied in the 1970s. In the 1980s, systems became the four- and five-component SS [13–16]. A study and application of lead-free materials based on ((Na,Li)NbO₃, (Na, K)NbO₃ (KNN) started in the 1990s due to ecological matters. The Restriction of Hazardous Substances Directive (RoHR) was officially adopted in 2003 in the European Union; it forbade use of lead in electronic devices [17], thus lead-free materials became very relevant. The multicomponent lead-free KNN niobate materials prevailed in the 2000s [18–21]. Saito et al. have proved in 2004 [22] that a KNN-based textured ceramic has a very high d₃₃₃ value (d₃₃₃ = 416 pC/N). The authors of [23] have revealed a twice larger d₃₃₃ value in this material. Lead-free KNN materials were intensely modified and became multi-element complex compounds in the 2010s [24,25]. The 2020s are marked by the modification of the KNN with rare earth elements (REEs) and the development of the new lead-free complex compositions, including the compounds with fundamentally different properties [26–29].

Thus, current material science develops in several directions: technology becomes greener; basic compositions of functional materials are complicated; non-isostructural components are incorporated into the initial systems; matrices are doped with exotic modifiers.

This is made to establish and integrate in materials various macro-responses, such as ferroelectric, piezoelectric, thermophysical, mechanical, luminescent, etc. All the above-mentioned modifications expand application possibilities of such multifunctional materials.

This work researches solid solutions (SSs) with the composition $\text{Na}_{0.90}\text{K}_{0.05}\text{Cd}_{0.05}\text{NbO}_3$. The SSs belong to the class of complex ferroelectric perovskites [30] of the ABO_3 type. The $\text{Na}_{0.90}\text{K}_{0.05}\text{Cd}_{0.05}\text{NbO}_3$ SS structure contains cuboctahedron voids (AO_{12} polyhedra). Voids can be occupied by several types of cations [31]. At this, sizes of cations can be other than the sizes of the polyhedra they occupy. As a result, interatomic bonds strain, and perfect perovskite subcells are significantly distorted. This leads to deformation and rotation of anionic octahedra in NaNbO_3 -based SSs [32,33]. A wide variety of both crystal lattice distortions and physical properties depend on the temperature and composition in NaNbO_3 -based SSs, which is rare among perovskite-type materials. The initial compound NaNbO_3 exhibits a number of structural phase transitions [34,35]. This crystallochemical feature causes the above-mentioned dependence. NaNbO_3 -based SS is characterized by the concentration and temperature phase transitions of the displacement type. Some of the phase transitions are associated with a change in the type of dipole ordering or with morphotropic regions of coexistence of phases characterized by differently ordered structure distortions [36,37]. The characteristics of morphotropic regions, the structures of individual phases, and their properties (including mechanical ones) depend on the microhomogeneity and the degree of structural ordering of these SSs. This is the reason why SSs are sensitive to the conditions of sample preparation.

Mechanical (for example, elastic) properties are crucial for the study of solids. Young's modulus characterizes interatomic interactions and macroscopic anisotropy of a solid. Elastic constants reveal many fundamental features of the interaction of particles in matter; the constants determine the P and T regions of phonon instability of the crystal lattice and much more.

The aim of this work is to expand the number of known properties of ceramics based on NaNbO_3 . In order to achieve this aim, we have synthesized multicomponent ceramic ferroelectric $\text{Na}_{0.90}\text{K}_{0.05}\text{Cd}_{0.05}\text{NbO}_3$ SSs doped with 5 mol% REE (La, Pr, Tb, Dy, Ho). We have studied their structure, microstructure, dielectric, thermophysical, and optical (luminescent) characteristics. The performed study has widened potential application of $[(\text{Na}_{0.90}\text{K}_{0.05}\text{Cd}_{0.05})_{0.95}\text{REE}_{0.05}]\text{NbO}_3$ SSs compared to the application range of the initial undoped $\text{Na}_{0.90}\text{K}_{0.05}\text{Cd}_{0.05}\text{NbO}_3$ SSs.

2. Materials and Methods

2.1. Materials

The objects of study were the SSs of the composition $\text{Na}_{0.90}\text{K}_{0.05}\text{Cd}_{0.05}\text{NbO}_3$ and $[(\text{Na}_{0.90}\text{K}_{0.05}\text{Cd}_{0.05})_{0.95}\text{REE}_{0.05}]\text{NbO}_3$, where REE = La, Pr, Tb, Dy, Ho. SSs were synthesized in accordance with the specified composition. The following initial components were mixed: sodium bicarbonate (NaHCO_3 , 99.9 (not more than 10^{-5} of 27 impurities), Komponent-reaktiv Ltd., Russia), potassium bicarbonate (KHCO_3 , 99.9%, Solikamsk Magnesium Plant, Russia), niobium (Nb_2O_5 , 99.9%, Solikamsk Magnesium Plant, Russia), and cadmium oxides (CdO , 99%). The lanthanum (La_2O_3 , 99.9, Himkraft, Russia), praseodymium (Pr_2O_3 , 99.9, Himkraft, Russia), terbium (Tb_2O_3 , 99.9, Himkraft, Russia), dysprosium (Dy_2O_3 , 99.9, Himkraft, Russia), and holmium (Ho_2O_3 , 99.9, Himkraft, Russia) oxides were used as the modifying dopants.

The samples were obtained by the two-stage solid-phase synthesis ($T_{\text{synt.1}} = 1020$ K, $\tau = 5$ h; $T_{\text{synt.2}} = 1070$ K, $\tau = 5$ h). After that the $\varnothing 10$ mm and 8–10 mm high blanks were sintered and treated by uniaxial hot pressing (UHP). Pressure was applied externally using the modernized installation for uniaxial hot pressing [38]. The optimal sintering modes for the UHP technology were determined: $T_{\text{sint}} = 1460$ K, $P = 230$ kg/cm², and $\tau_{\text{sint}} = 60$ min. The pressure was applied at room temperature and maintained at the stages of the temperature rise and isothermal holding. The applied pressure was removed during cooling. The preparation modes were optimized for each composition: the sintering temperature

varied in a series of samples. Phase composition of the synthesized and sintered blanks was controlled with the XRD. Additionally, the microstructure was analyzed and the ceramics density was determined. The selected technology regulations were obtained on the basis of these results. The technology ensured the absolute purity or minimization of the ballast phases in synthesized powders and sintered ceramics. Ballast phases cannot be completely excluded within the applied method of the SSs preparation. The technology also ensured the high density, a sufficiently high quality of their microstructure, and the integrity and intactness of the ceramic frame.

The sintered ceramic blanks were mechanically treated: cut along the plane, grinded and polished along the flat surfaces and ends. As a result, samples were $\varnothing 10 \text{ mm} \times 1 \text{ mm}$. Each composition provided 8–10 sample pieces. Before the metal spraying, the samples were calcined at $T_{\text{calc.}} = 770 \text{ K}$ for 0.5 h to remove the organic residues and degrease the surfaces in order to increase the adhesion of the metal coating to the ceramics. The electrodes were applied by the double firing of a silver-containing paste onto the flat sample surfaces at 1070 K for 0.5 h.

2.2. Research

The XRD studies were performed by the powder diffraction on a DRON-3 diffractometer (NPP Burevestnik, St. Petersburg, Russia, 2012) with an IR-2 X-ray interferometer (Radicon Ltd., St. Petersburg, Russia) using $\text{CoK}\alpha$ radiation. The IR-2 was connected to a computer equipped with special programs. Parameters of the perovskite cell and the uniform deformation parameter δ were calculated. The deformation parameter characterizes the spontaneous deformation value. Calculation formulas corresponded to the monoclinic symmetry of the crystal lattice. Formulas were simplified, taking into account the small deviation of the perovskite cell from the cubic one [38]:

$$d_{hkl} = \frac{a \sin \beta}{\sqrt{N}} \left(1 + \frac{k^2}{N} y + \frac{lh}{N} \cos \beta \right) \quad (1)$$

$$\delta = \frac{a \sqrt{1 - \cos \beta}}{\bar{a}} - 1 \quad (2)$$

where $N = h^2 + k^2 + l^2$; h, k, l —the diffraction indices; $y = (b/a \sin \beta) - 1$; a, b, β —the parameters of the perovskite cell; $\bar{a} = \sqrt[3]{V}$ —the average parameter. The monoclinic (M) unit cell parameters were calculated from the diffraction peaks 200, 020, and 22 $\bar{2}$. The measure errors for the structural parameters were as follows: $\Delta a = \Delta b = \Delta c = \pm 0.004 \text{ \AA}$, $\Delta \beta = \pm 0.05^\circ$, and $\Delta V = \pm 0.10 \text{ \AA}^3$.

The experimental density of the samples was measured by hydrostatic weighing in octane. The XRD density was calculated by the formula: $\rho_{\text{x-ray}} = 1.66 \cdot M/V$, where M is the molecular weight per cell, and V is the volume of the cell. Integral density was measured for every sample obtained from the same sintered blank. This confirmed a high homogeneity of the samples under study and the reliability of the results obtained in the work.

The microstructure of the ceramic chips was studied by a JSM-6390L scanning electron microscope (JEOL Ltd., Tokyo, Japan, 2003) with an AZtecLive microanalyzer system (Oxford Instruments, High Wycombe, Great Britain). The microscope resolution was up to 1.2 nm at an accelerating voltage of 30 kV for the image in the secondary electrons, the accelerating voltage range was from 0.5 to 30 kV, the magnification was from $\times 10$ to $\times 1,000,000$, and the beam current was up to 200 nA. The study of the morphology was performed using a VK-9700 color laser scanning 3D microscope (KEYENCE, Itasca, IL, USA) and a TM1000 electron microscope (Hitachi, Tokyo, Japan).

The temperature dependences of real and imaginary parts of the relative complex permittivity were obtained using a measuring stand based on an Agilent 4980 A LCR-meter (Agilent Technologies, USA, Santa Clara, 2008). The temperature was measured at $T = 300\text{--}900 \text{ K}$ and in the frequency range $f = 25\text{--}1 \times 10^6 \text{ Hz}$. By real and imagi-

nary parts of the relative complex permittivity we mean $\varepsilon^*/\varepsilon_0 = \varepsilon'/\varepsilon_0 - i\varepsilon''/\varepsilon_0$, where $\varepsilon_0 = 8.75 \cdot 10^{-12}$ F/m—the dielectric constant of the samples.

Low-temperature dielectric measurements were carried out in the temperature range $T = 10\text{--}300$ K at frequencies $f = 20\text{--}1 \times 10^6$ Hz using a Wayne Kerr 6500 B precision impedance analyzer (Wayne Kerr Electronics, UK, Bognor Regis, 2006). The samples were cooled using a CCS-150 Cryogenics closed-type helium refrigeration cryostat (Lake Shore Cryotronics Inc., Westerville, OH, USA). The temperature was controlled using a Model 331 temperature controller (Lake Shore Cryotronics Inc., Westerville, OH, USA). We were able to maintain the set temperature with an accuracy of ± 0.01 K. During measurements, the samples were placed in the vacuum chamber of the cryostat; the vacuum was created by a BOC turbomolecular pump (Edwards, Stockholm, Sweden).

The thermal expansion ($\Delta L/L$) and the linear coefficient of the thermal expansion (α) were studied using a specially designed measuring installation based on a MICRON-02 device for checking the end rods ("TOT" Enterprise, Russia, Yaroslavl, 2010), and an nanovoltmeter/microohmmeter Agilent 34420A (Agilent Technologies, USA, Santa Clara, 2012). The sensitivity to the displacement was 10^{-8} m, and the measurement error was 4%. The temperature in the chamber was changed at a rate of $\Delta T = 1$ K/min.

The mechanical properties of the ceramics were investigated by the contact method on a NanoScan probe microscope–nanohardness tester (FSBI TISNCM, Troitsk, Russia).

The photoluminescence (PL) spectra of the studied ceramic samples were recorded using a SOL SL-100M spectrograph (SOL instruments, Belarus, Minsk) with an FLI ML 1107 Black Illuminated CCD detector (Hamamatsu PHOTONICS K.K., Japan, Hamamatsu City) in the spectral range 380–800 nm. The entrance slit of the monochromator was 0.4 mm. A He-Cd continuous laser (Kimmon KOHA, Japan, Fukushima) set to $\lambda_0 = 325$ nm and $P = 15$ mW was used as a luminescence excitation source. Each PL spectrum was corrected to the background signal.

3. Results and Discussion

3.1. X-Ray Study

The initial $\text{Na}_{0.90}\text{K}_{0.05}\text{Cd}_{0.05}\text{NbO}_3$ SS crystallizes in a perovskite-type structure; it has the rhombic symmetry with a monoclinically distorted perovskite cell. The correlations between the parameters of the monoclinic cell $a = c > b$ and $\alpha = \gamma < \beta$, and the rhombic cell A , B , and C are as follows: $A = 2a \cos \beta/2$, $B = 2b$, and $C = 2a \sin \beta/2$. Figure 1 shows the XRD patterns of the initial $\text{Na}_{0.90}\text{K}_{0.05}\text{Cd}_{0.05}\text{NbO}_3$ (curve 1) and the modified $[(\text{Na}_{0.90}\text{K}_{0.05}\text{Cd}_{0.05})_{0.95}\text{REE}_{0.05}]\text{NbO}_3$, REE = La, Pr, Tb, Dy, Ho (2, 3, 4, 5, 6, respectively) SSs. The peaks are characterized by the data available from [39].

The XRD pattern of the $\text{Na}_{0.90}\text{K}_{0.05}\text{Cd}_{0.05}\text{NbO}_3$ SS shows the splitting of the multiplets corresponding to the monoclinic distortion of the perovskite cell. The basic NaNbO_3 compound in Figure 1a (1) corresponds to card (JCPDS 14-603). This card was used because KNbO_3 and CdNb_2O_6 are only 5% in the base SS. A very weak superstructural peak (marked with an asterisk) indicates a doubling of the b axis.

The XRD patterns of the modified SSs show that the modification with the La^{3+} and Pr^{3+} ions changes the crystal lattice symmetry. The multiplet 200, 020 becomes almost a single peak, and the symmetry increases to the pseudocubic (PsC) one (the XRD patterns 2, 3, Figure 1). The absence of the impurities, the change in the symmetry, and the slight increase in the volume of the perovskite cell (Table 1) indicate that the large-sized La^{3+} and Pr^{3+} ions successfully incorporate into the crystal lattice of the initial SS. It should be noted that an increase in the cell volume is possible only with the substitution $(\text{La}^{3+}, \text{Pr}^{3+}) \rightarrow \text{Na}^+$ (1.04, 1.00, and 0.98, respectively): the ionic radius of K^+ (1.33) is much larger than the radii of La^{3+} and Pr^{3+} ; cadmium and these REEs have a large difference in the electronegativities ($\text{Cd} = 1.69$, $\text{La} = 1.1$, and $\text{Pr} = 1.13$), which prevents them from replacing cadmium [40]. The REEs Tb, Dy, and Ho do not completely incorporate into the crystal lattice of the initial SS, but form the impurity LnNbO_4 compounds of the monoclinic fergusonite type. As the ionic radii of the REEs decrease in the row $\text{Tb} \rightarrow \text{Dy} \rightarrow \text{Ho}$, the intensity of the XRD peaks of

the impurity compound in the XRD patterns 4–6 (Figure 1) increases, and the symmetry of the SS again becomes monoclinic. A single XRD peak 200 on the XRD patterns 2 and 3 (Figure 1) is again transformed into the multiplet 200, 020 (Figure 1: patterns 4, 5, and 6). The volume of the perovskite unit cell (Table 1) decreases in accordance with a decrease in the ionic radii of REEs.

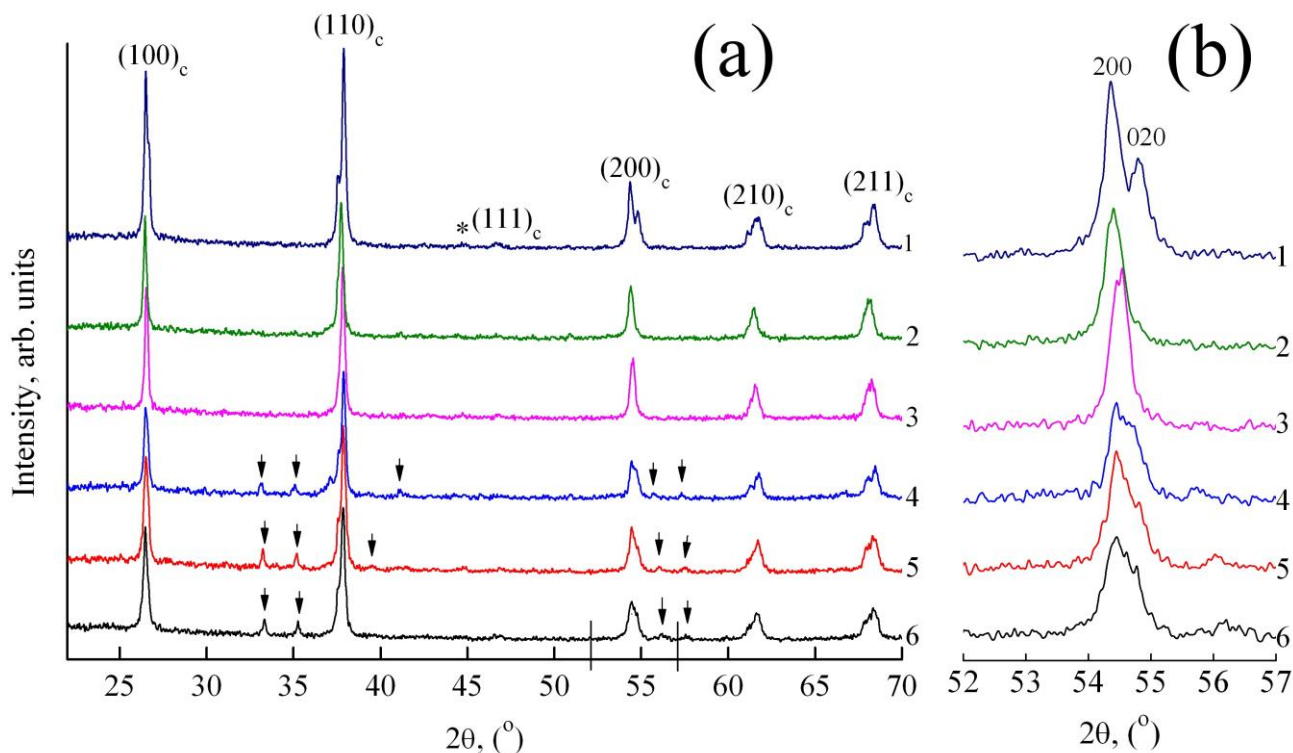


Figure 1. (a) XRD patterns of the studied SSs: (1)—the initial and modified with (2) La; (3) Pr; (4) Tb; (5) Dy; (6) Ho. Indices $(hkl)_c$ correspond to the perovskite axes. The arrows mark the peaks of the impurity phases: TbNbO_4 (4) (JCPDS 23-1417), DyNbO_4 (5) (JCPDS 22-1094), and HoNbO_4 (6) (JCPDS 23-1104). The asterisk marks a very weak superstructural peak indicating the doubling of the b axis. (b) The diffraction peaks (200) and (020) are enlarged along the 2θ axis.

Table 1. The symmetry and parameters of the perovskite cell of the initial and modified by the REE $\text{Na}_{0.9}\text{K}_{0.05}\text{Cd}_{0.05}\text{NbO}_3$ SS; experimental (ρ_{exp}) and relative (ρ_{rel}) densities of the ceramic samples.

Composition	Symmetry	$a = c, \text{ \AA}$	$b, \text{ \AA}$	β ($^\circ$)	$V, \text{ \AA}^3$	$\rho_{\text{exp}}, \text{ g/cm}^3$	$\rho_{\text{rel}}, \%$
$\text{Na}_{0.9}\text{K}_{0.05}\text{Cd}_{0.05}\text{NbO}_3$	M	3.922	3.893	90.26	59.9	4.59	99.6
$[(\text{Na}_{1-x-y}\text{K}_x\text{Cd}_y)_{0.95}\text{La}_{0.05}]\text{NbO}_3$	PsC	3.921			60.3	4.58	100
$[(\text{Na}_{1-x-y}\text{K}_x\text{Cd}_y)_{0.95}\text{Pr}_{0.05}]\text{NbO}_3$	PsC	3.916			60.03	4.62	100
$[(\text{Na}_{1-x-y}\text{K}_x\text{Cd}_y)_{0.95}\text{Tb}_{0.05}]\text{NbO}_3$	M	3.921	3.903	90.43	60.0	4.54	98.2
$[(\text{Na}_{1-x-y}\text{K}_x\text{Cd}_y)_{0.95}\text{Dy}_{0.05}]\text{NbO}_3$	M	3.921	3.896	90.54	59.9	4.77	102
$[(\text{Na}_{1-x-y}\text{K}_x\text{Cd}_y)_{0.95}\text{Ho}_{0.05}]\text{NbO}_3$	M	3.921	3.899	90.54	59.96	4.73	102

Thus, the precipitation of medium-sized REE ions Tb, Dy, and Ho into the impurity, the return of monoclinic distortion, and a slight decrease in the volume of the perovskite cell indicate that these REEs do not completely incorporate in the original SS. In this case, the profile of the diffraction peak (200) in XRD pattern 5 (Figure 1) and the smallest cell volume (Table 1) indicate that among medium-sized REEs, Dy incorporates into the crystal lattice of the initial SS easier and forms the most homogeneous SS.

Table 1 shows the symmetry and parameters of the perovskite cell of the initial and modified with the REEs SSs based on $\text{Na}_{0.9}\text{K}_{0.05}\text{Cd}_{0.05}\text{NbO}_3$, as well as the experimental and relative density of the ceramic samples.

The relative density above 100% can be due to the fact that the measurement of the experimental density in the samples containing the second phase cannot separate the contribution of each phase to the density of the bulk sample. Qualitatively, this can be explained by the fact that the heavy REE ions do not incorporate into the SS; they form instead the LnNbO_4 impurity compound. The compound has a much higher density ($7.0\text{--}7.3\text{ g/cm}^3$) than the initial SS. Therefore, the average experimental density of the sample is overestimated. Since the X-ray density is calculated for a stoichiometric SS, the relative density of the sample can exceed 100%.

3.2. Microstructure

The main characteristic of the microstructure of the ceramics is the average grain size \bar{D} . Its value is in a good agreement with the XRD data. Thus, an increase in δ in the samples with Tb, Dy, and Ho leads to a sharp refinement of the morphology due to the existing inverse dependence of \bar{D} on δ ($\bar{D} \sim 1/\delta$ [41]). The fact that the compositions with a large δ have a smaller crystallite size can be explained by an increase in the internal stresses in the ceramics with an increase in the spontaneous deformation. It is these stresses that inhibit the growth of the crystallites [41].

An additional factor, which, in our opinion, is also associated with the formation of the fine-grained structures in these samples, as well as in La- and Pr-containing ones, may be the polymorphism of the initial reagents—the REE (Ln_2O_3) oxides. The oxides undergo a series of the phase transformations during the heat treatment of the charge. At low temperatures ($\sim 400\text{ K}$), oxides interact with water and form $\text{Ln}(\text{OH})_3$ hydrates; at higher temperatures ($\sim 470\text{--}1170\text{ K}$) oxides decompose [42]. These circumstances are associated with the Hedvall effect—an increase in the reactivity of the solids during or as a result of the polymorphic transformations [43]. This, in turn, causes the simultaneous formation of many centers of the primary recrystallization with the reduced mass capacity; as a result, smaller crystallites grow from each nucleus, forming a new grain pattern. It should be noted that impurities can act as such crystallization centers; the impurities form during the modification of the SS with the low-sized REEs (Tb, Dy, Ho).

As the ionic radii of the REE decreases in the row La→Ho, surface charge density increases; thus, hydration energy on cations increases. Hydration energy is the energy released when interacting with water molecules. As a result, the most significant refinement of the grain structures should be observed in the samples with medium-sized Tb, Dy, and Ho; and they were observed.

In the initial and modified samples, grains crystallize in the form of almost regular geometric figures: parallelepipeds or plates for larger grains; almost regular cubes for smaller grains (Figure 2). This indicates that the crystallization takes place in the presence of the liquid phases, not in the solid phase [41]. The unreacted initial reagents with low melting points and low-melting eutectics in the charges of alkali metal niobates can serve as sources of liquid phases: Na_2O with $T_{\text{melt}} = 1405\text{ K}$; K_2O with $T_{\text{melt}} = 1013\text{ K}$; CdO with $T_{\text{melt}} = 1173\text{ K}$; Na_2CO_3 with $T_{\text{melt}} = 1127\text{ K}$; K_2CO with $T_{\text{melt}} = 1164\text{ K}$; Li_2CO_3 with $T_{\text{melt}} = 1005\text{ K}$; NaOH with $T_{\text{melt}} = 596\text{ K}$; KOH with $T_{\text{melt}} = 678\text{ K}$; NaNbO_3 with $T_{\text{melt}} = 1695\text{ K}$; KNbO_3 with $T_{\text{melt}} = 1373\text{ K}$, etc.

The ceramic sample of the initial composition $\text{Na}_{0.9}\text{K}_{0.05}\text{Cd}_{0.05}\text{NbO}_3$ is quite different from REE-modified ones (Figure 2a). Its microstructure has no separate grains. The surface of the initial ceramics has a stepped-layered structure fragment (circled by the dashed line on the Figure 2a), which is somewhat unusual. This is probably a manifestation of the linear stacking faults that contain dislocation motives with the steps. The steps are the result of the precipitation of the excess vacancies. The vacancies appear due to the high volatility of the alkali metals; the other reason for vacancies' appearance is two parts of the stacking faults moving in different directions. A set of such periodically arranged dislocations forms both grain boundaries and ensembles of grain boundaries in the considered SSs. Usually, dislocation motives with the steps are destroyed during recrystallization [42]; in our case they are retained during annealing after the plastic deformation. This, apparently, is a

consequence of the externally applied pressure during the sintering of SSs, which fixes these stacking faults.

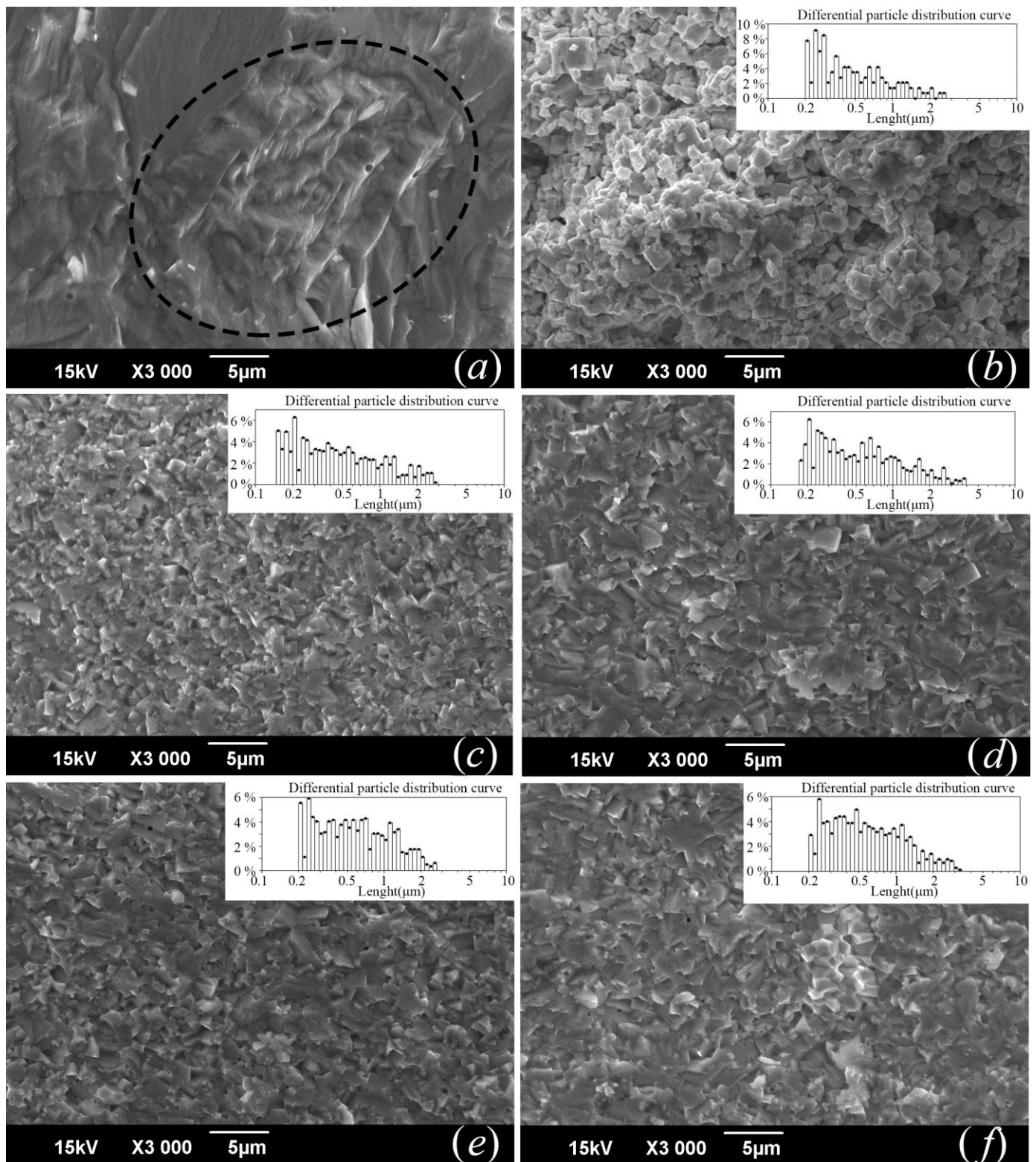


Figure 2. SEM images of transverse cleavage of ceramic SSs: (a) of the initial one and modified with (b) La; (c) Pr; (d) Tb; (e) Dy; (f) Ho. Insets demonstrate differential curves of ceramic grain size distribution in corresponding composition of SS.

A similar situation, but on a smaller scale, takes place in the samples with Tb, Dy, and Ho (Figure 2c–e). The effect is absent from the La-modified SSs (Figure 2b). Differential curves of ceramic grain size distribution shown on insets of Figure 2b–f demonstrate that microstructure grains have sizes 0.15–2.5 μm . The average grain size (from 400 to 550 nm) increases in the REE-doped SSs in the dopant row La \rightarrow Ho. Ceramic grains often do not have clear boundaries and the adhesion between crystallites is quite high. Pores are almost absent.

The observed facts confirm the earlier statement: the large-sized (La and Pr) REEs incorporate into the base crystal lattice completely and stabilize the lattice; the medium-sized Tb, Dy, and Ho on the contrary incorporate into the initial structure only partially. As a result, the lattice does not even change its symmetry.

3.3. Dielectric Properties

Figures 3 and 4 shows the dependences of ϵ'/ϵ_0 and ϵ''/ϵ_0 on the temperature at the various frequencies of the alternating electric field obtained in the studied samples cooling mode.

The ceramics of the initial SS composition $\text{Na}_{0.90}\text{K}_{0.05}\text{Cd}_{0.05}\text{NbO}_3$ has two peaks of the permittivity constant (Figure 3a). They correspond to the transition from the orthorhombic (O) phase to the tetragonal (T) one (T_{O-T}), and from the tetragonal phase to the cubic one (T_{T-C}) [44]. The dispersion of the dielectric constant begins to manifest itself only above T_{T-C} (Figure 3a).

The introduction of REE dopants with $R \geq 1.0 \text{ \AA}$ (Pr and La in Figure 3b,c) shifts T_{O-T} and T_{T-C} to the low-temperature region [45]; the same happens with the convergence of T_{O-T} and T_{T-C} upon doping with REE $R < 0.92 \text{ \AA}$ (Tb, Dy, and Ho in Figure 4), which may be due to a decrease in the lattice stability [46]. The shift might be caused by the increase in the disorder in the case of heterovalent substitution in the A-sublattice. In our case, when REEs with $R \geq 1.0 \text{ \AA}$ are introduced, one can see the following: $T_C \sim 410 \text{ K}$ for La (Figure 3b) and $T_C \sim 340 \text{ K}$ for Pr (Figure 3c).

At $R < 0.92 \text{ \AA}$ (Tb, Dy, and Ho), T_C is in the range (500–550) K (Figure 4). The temperature range is so wide in SSs modified with Dy and Ho due to the formation of two small maxima of ϵ'/ϵ_0 forming together a quasi-plateau region (Figure 4b,c). The latter may be due to the manifestation of the O \rightarrow T and T \rightarrow C phase transitions in the base compounds, which are shifted towards each other and form the indicated anomaly [44]. However, this phenomenon requires additional research. In the paraelectric region, ϵ'/ϵ_0 and ϵ''/ϵ_0 significantly increase with increasing the temperature (Figure 4). This might be caused by the increasing contribution of the through electrical conductivity to ϵ'/ϵ_0 and ϵ''/ϵ_0 dependences. The through electrical conductivity is most likely caused by the redox processes in the ceramics, provoked by the presence of the Nb ions in their compositions; Nb has a variable valence.

The introduction of the REEs blurs ϵ'/ϵ_0 and ϵ''/ϵ_0 maxima at the T_{T-C} transition in a quite wide temperature range (Figures 3 and 4, insets in column 1). Thereby, only the unmodified SS with the $\text{Na}_{0.9}\text{K}_{0.05}\text{Cd}_{0.05}\text{NbO}_3$ composition (the inset in Figure 3(a1)) in the paraelectric phase obeys the empirical Curie-Weiss law, $\epsilon'/\epsilon_0 = C/(T - T_C)$, where the Curie-Weiss constant $C = 1.27 \cdot 10^5 \text{ K}$, and the Curie-Weiss temperature $T_C = 633 \text{ K}$. The measuring field frequency of 520 kHz was chosen to eliminate the contribution of the space charge polarization at high temperatures.

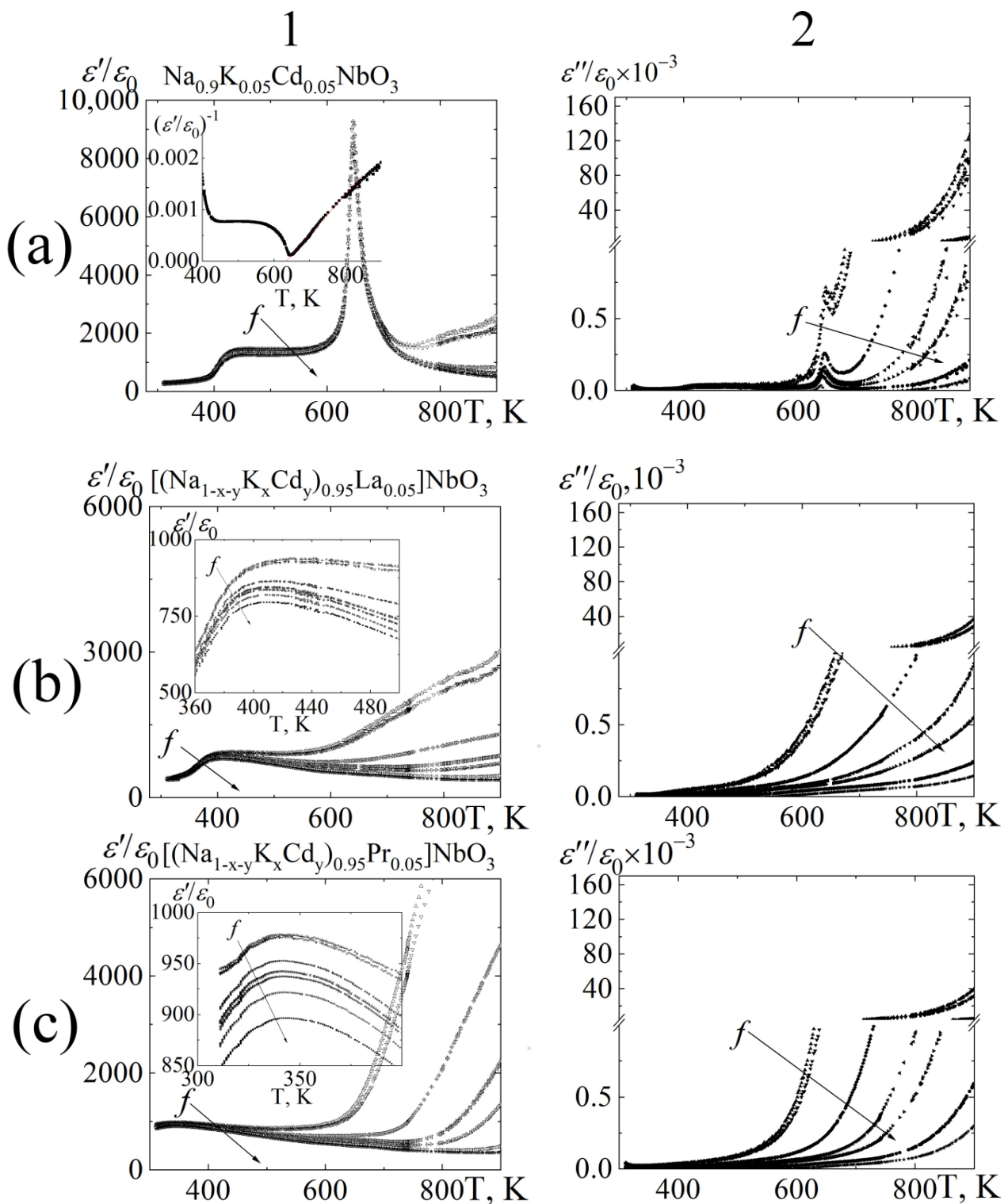


Figure 3. Column (1): dependence of ϵ'/ϵ_0 ; column (2): dependence of ϵ''/ϵ_0 on the temperature at different frequencies (f) of the alternating electric field obtained in the cooling mode of the samples, in temperature range of $T = (300\text{--}900)$ K: (a) $\text{Na}_{0.90}\text{K}_{0.05}\text{Cd}_{0.05}\text{NbO}_3$; (b) $[(\text{Na}_{1-x-y}\text{K}_x\text{Cd}_y)_{0.95}\text{La}_{0.05}]\text{NbO}_3$; (c) $[(\text{Na}_{1-x-y}\text{K}_x\text{Cd}_y)_{0.95}\text{Pr}_{0.05}]\text{NbO}_3$. The inset in a(1) shows dependences $(\epsilon'/\epsilon_0)^{-1}(T)$ to demonstrate the empirical Curie-Weiss law. The insets in b(1) and c(1) show the dispersion and blurring of ϵ'/ϵ_0 at the instant of the phase transition. The arrow shows the direction of f increase. Frequencies are denoted as follows: Δ $8 \cdot 10^2$ Hz; ∇ $1.0 \cdot 10^4$ Hz; \diamond $1.0 \cdot 10^5$ Hz; ⋈ $5.2 \cdot 10^5$ Hz; \triangleright $2.5 \cdot 10^6$ Hz; \diamond $7.2 \cdot 10^6$ Hz; \star $1.2 \cdot 10^7$ Hz.

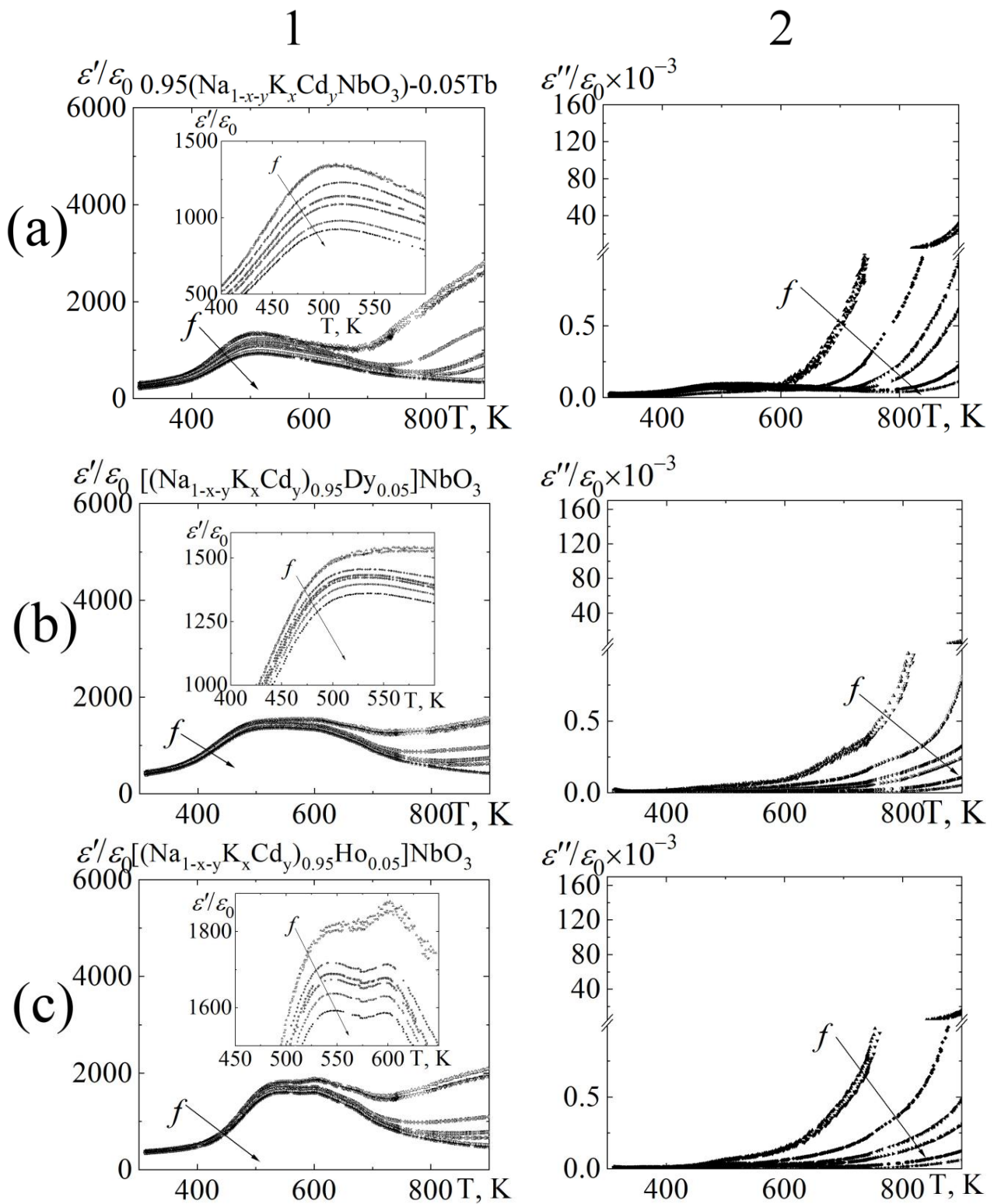


Figure 4. Column (1): dependence of ϵ'/ϵ_0 ; column (2): dependence of ϵ''/ϵ_0 on the temperature at different frequencies (f) of the alternating electric field obtained in the cooling mode of the samples, in temperature range of $T = (300\text{--}900)$ K: (a) $[(\text{Na}_{0.90}\text{K}_{0.05}\text{Cd}_{0.05})_{0.95}\text{Tb}_{0.05}]\text{NbO}_3$; (b) $[(\text{Na}_{0.90}\text{K}_{0.05}\text{Cd}_{0.05})_{0.95}\text{Dy}_{0.05}]\text{NbO}_3$; (c) $[(\text{Na}_{0.90}\text{K}_{0.05}\text{Cd}_{0.05})_{0.95}\text{Ho}_{0.05}]\text{NbO}_3$. The insets in column (1) show the dispersion and blurring of ϵ'/ϵ_0 at the instant of the phase transition. The arrow shows the direction of f increase. Frequencies are denoted as follows: $\triangle 8 \cdot 10^2$ Hz; $\nabla 1.0 \cdot 10^4$ Hz; $\diamond 1.0 \cdot 10^5$ Hz; $\otimes 5.2 \cdot 10^5$ Hz; $\triangleright 2.5 \cdot 10^6$ Hz; $\oplus 7.2 \cdot 10^6$ Hz; $\star 1.2 \cdot 10^7$ Hz.

To confirm the possible shift of T_{O-T} and T_{T-C} to different temperature ranges depending on the REE size, we additionally studied ϵ'/ϵ_0 and ϵ''/ϵ_0 in the range (10–325) K (Figures 5 and 6). It has been established that the formation of a quasi-maximum at ~ 245 K is typical for the basic SS $\text{Na}_{0.9}\text{K}_{0.05}\text{Cd}_{0.05}\text{NbO}_3$ (Figure 5a). The quasi-maximum may be explained by the $T_R \rightarrow T_O$ transition in the basic system (Na, K) NbO_3 [47]. A similar effect was observed in the $(\text{K}_{0.48}\text{Na}_{0.52})(\text{Nb}_{1-x}\text{Sb}_x)\text{O}_3$ system [48]. A clearly pronounced hysteresis of the permittivity ϵ'/ϵ_0 manifests at $T \sim (200\text{--}320)$ K (inset on Figure 5(a1)), while ϵ''/ϵ_0 decreases without any anomalies in the entire temperature range. However, a weak dispersion ϵ'/ϵ_0 and ϵ''/ϵ_0 is observed at $T \sim (220\text{--}320)$ K, while it is almost absent above 320 K. The introduction of large-sized La (Figure 5(b1)) suppressed the indicated ϵ'/ϵ_0 anomaly, i.e., any inflection points are absent. However, it is necessary to note a weak hysteresis at $T \sim (200\text{--}320)$ K (inset in Figure 5(b1)). The dispersion of ϵ'/ϵ_0 and ϵ''/ϵ_0 remains unchanged at $T < 200$ K of La-modified $\text{Na}_{0.9}\text{K}_{0.05}\text{Cd}_{0.05}\text{NbO}_3$ (Figure 5b). At $T > 200$ K a rapid increase in $(\epsilon'/\epsilon_0, \epsilon''/\epsilon_0)(T)$ is observed: the lower is the frequency of the measuring electric field, the stronger the increase is. SS containing Pr (Figure 5c) is characterized by an increase in ϵ'/ϵ_0 and a decrease in ϵ''/ϵ_0 at $T \sim (10\text{--}260)$. An inflection point forms at $T \sim 260$ K. After that $\epsilon'/\epsilon_0(T)$ of Pr-modified $\text{Na}_{0.9}\text{K}_{0.05}\text{Cd}_{0.05}\text{NbO}_3$ demonstrates a plateau-like area at $T \sim (260\text{--}320)$ K and $\epsilon''/\epsilon_0(T)$ grows (Figure 5c). A weak hysteresis is present in the dependences $(\epsilon'/\epsilon_0$ and $\epsilon''/\epsilon_0)(T)$ up to the inflection point $T = 260$ K and increases at $T > 260$ K (Figure 5c). The dispersion of these dependences is observed over the entire temperature range of Pr-modified $\text{Na}_{0.9}\text{K}_{0.05}\text{Cd}_{0.05}\text{NbO}_3$ (Figure 5c).

Tb-modified SS has ϵ'/ϵ_0 and ϵ''/ϵ_0 maxima in the range (150–320) K of a relaxation nature: ϵ'/ϵ_0 and ϵ''/ϵ_0 shift to the region of higher temperatures with an increase in the frequency of the measuring field (Figure 6a). The introduction of small Dy and Ho ions (Figure 6b,c) caused a shift of the maximum observed in the SS $\text{Na}_{0.9}\text{K}_{0.05}\text{Cd}_{0.05}\text{NbO}_3$ (Figure 5a) to the low-temperature region ($T \sim 200$ K). In Dy- and Ho-modified $\text{Na}_{0.9}\text{K}_{0.05}\text{Cd}_{0.05}\text{NbO}_3$ the hysteresis decreases to this region, and dispersion of $(\epsilon'/\epsilon_0, \epsilon''/\epsilon_0)(T)$ stays almost unchanged over the entire low-temperature range under study (Figure 6b,c).

Considering the significant blurring of the T_{T-C} transition, the modified Curie-Weiss law was used to characterize it [49]:

$$\frac{1}{\epsilon} - \frac{1}{\epsilon_m} = \frac{(T - T_m)^\gamma}{C}, \quad (T > T_m), \quad (3)$$

where ϵ_m —the dielectric constant at T_m , C is assumed to be the constant, and γ —the degree of the blurring, which can be in the range from 1 for a normal ferroelectric to 2 for an ideal relaxor ferroelectric [50,51]. Figure 7 shows the dependences of $\log(1/\epsilon' - 1/\epsilon_m)$ on $\log(T - T_m)$ obtained at a frequency of 520 kHz. All the samples, except those containing Ho and Dy, are characterized by a linear dependence. The slope of the approximating straight line was used to determine the parameter γ [50]. It was found that $\gamma \sim 1.7$ upon the modification of the initial SS with the REEs = La, Pr, and Tb. The obtained data indicate a diffuse phase transition. The shift of the maximum of the dielectric constant downward in the temperature indicates an increase in the conductivity in the studied SSs.

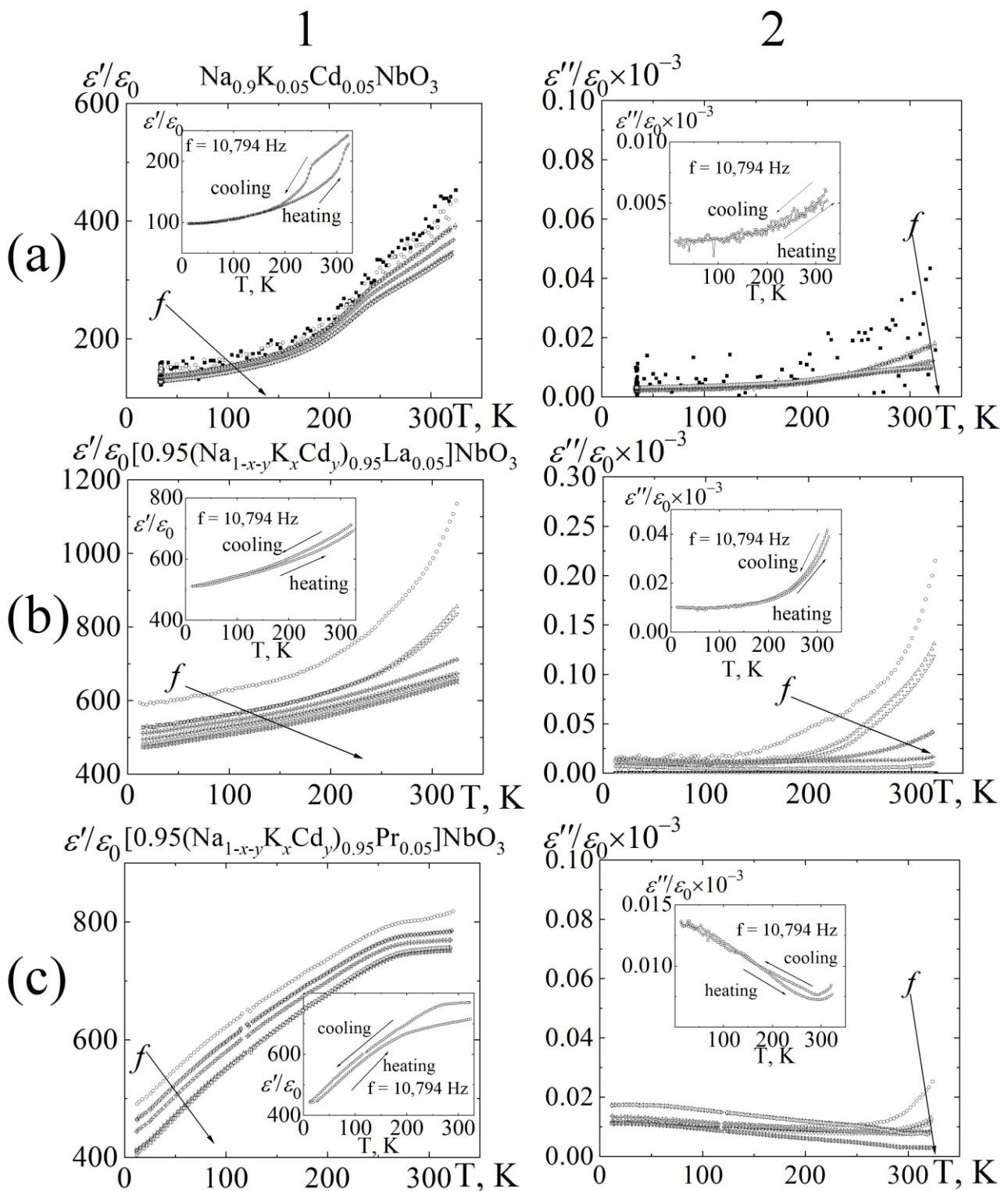


Figure 5. Column (1): dependence ϵ'/ϵ_0 , column (2): dependence ϵ''/ϵ_0 on the temperature at different frequencies (f) of the alternating electric field obtained in the cooling mode of the samples, in temperature range of $T = (10\text{--}325)$ K: (a) $\text{Na}_{0.90}\text{K}_{0.05}\text{Cd}_{0.05}\text{NbO}_3$; (b) $[(\text{Na}_{0.90}\text{K}_{0.05}\text{Cd}_{0.05})_{0.95}\text{La}_{0.05}]\text{NbO}_3$; (c) $[(\text{Na}_{0.90}\text{K}_{0.05}\text{Cd}_{0.05})_{0.95}\text{Pr}_{0.05}]\text{NbO}_3$. The insets in column (1) show the dispersion and blurring of ϵ'/ϵ_0 at the instant of the phase transition. The arrow shows the direction of f increase. Frequencies are denoted as follows: \circ 96 Hz; \triangle $8 \cdot 10^2$ Hz; ∇ $1.0 \cdot 10^4$ Hz; \diamond $1.0 \cdot 10^5$ Hz; \times $2.5 \cdot 10^5$ Hz; \triangleright $7.2 \cdot 10^6$ Hz; \oplus $7.2 \cdot 10^6$ Hz; \star $1.2 \cdot 10^7$ Hz.

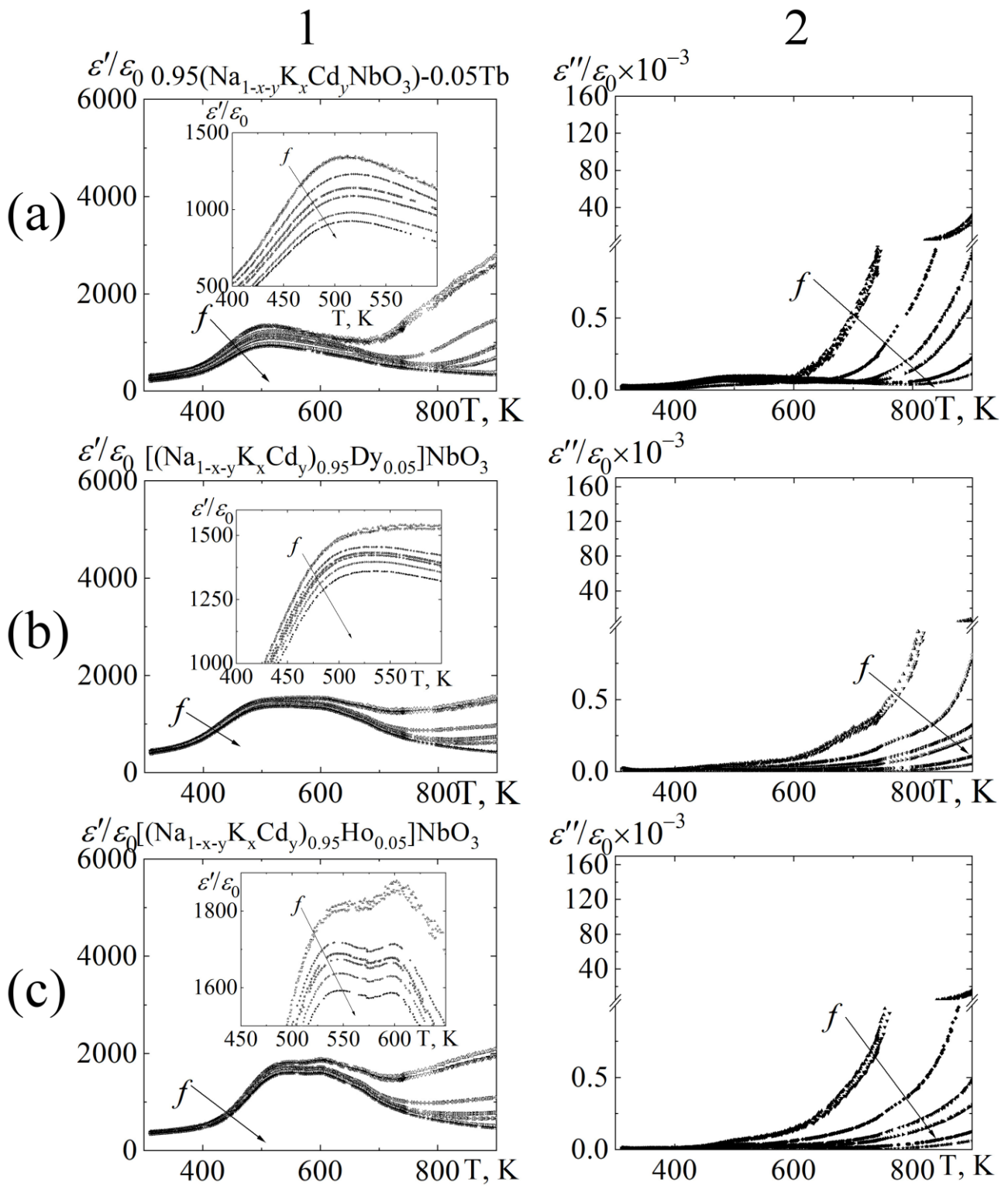


Figure 6. Column (1): dependence ϵ'/ϵ_0 , column (2): dependence ϵ''/ϵ_0 on the temperature at different frequencies of the alternating electric field obtained in the cooling mode of the samples, in temperature range of $T = (10\text{--}325)$ K: (a) $[(\text{Na}_{0.90}\text{K}_{0.05}\text{Cd}_{0.05})_{0.95}\text{Tb}_{0.05}]\text{NbO}_3$; (b) $[(\text{Na}_{0.90}\text{K}_{0.05}\text{Cd}_{0.05})_{0.95}\text{Dy}_{0.05}]\text{NbO}_3$; (c) $[(\text{Na}_{0.90}\text{K}_{0.05}\text{Cd}_{0.05})_{0.95}\text{Ho}_{0.05}]\text{NbO}_3$. The insets in column (1) show the dispersion and blurring of ϵ'/ϵ_0 at the instant of the phase transition. The arrow shows the direction of f increase. Frequencies are denoted as follows: \circ 96 Hz; \triangle $8 \cdot 10^2$ Hz; ∇ $1.0 \cdot 10^4$ Hz; \diamond $1.0 \cdot 10^5$ Hz; \otimes $2.5 \cdot 10^5$ Hz; \triangleright $7.2 \cdot 10^6$ Hz; \oplus $7.2 \cdot 10^6$ Hz; \star $1.2 \cdot 10^7$ Hz.

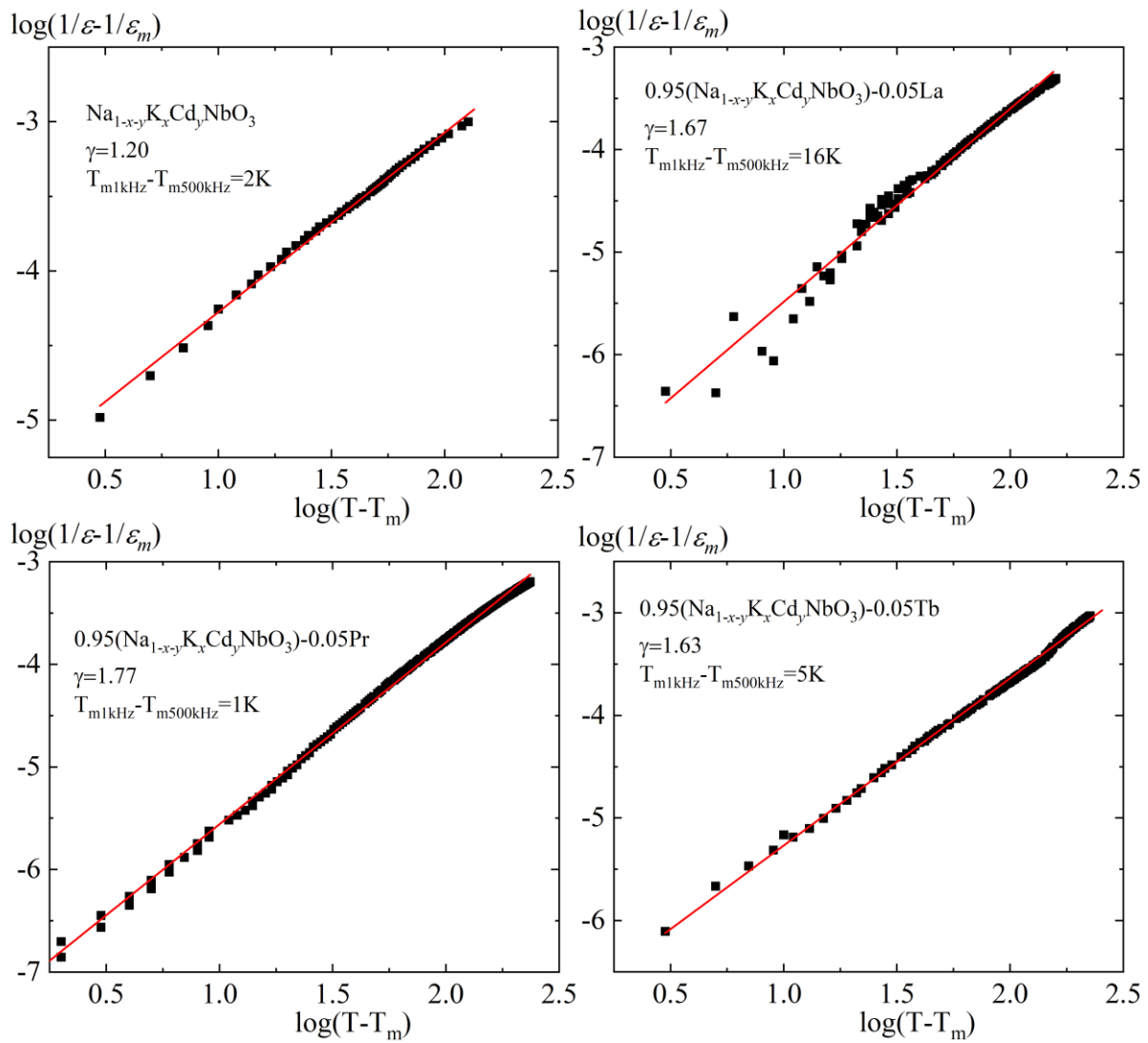


Figure 7. The dependence of $\log(1/\varepsilon - 1/\varepsilon_m)$ on $\log(T - T_m)$ for the investigated ceramic SSs. The solid line shows the result of the linear approximation.

3.4. Thermophysical Properties

Figures 8–10 show the dependences of $\varepsilon'/\varepsilon_0$ (the cooling mode), α , and $\Delta L/L$ on the temperature of the investigated ceramic SSs.

It was established that in the initial $\text{Na}_{0.90}\text{K}_{0.05}\text{Cd}_{0.05}\text{NbO}_3$ SS, $\Delta L/L(T)$, both upon heating and cooling, the slope changes for this dependence in the neighborhoods of T_{O-T} and T_{T-C} (Figure 8a). The line in Figure 8a shows the deviation from the linear law. It should be also noted that for other temperature ranges during cooling, the additional nonlinear dependences of the $\Delta L/L(T)$ are formed (Figure 8a). This indicates the presence of certain structural instabilities that do not significantly affect the dielectric properties, but apparently change the linear dimensions of the experimental sample. The dependence $\alpha(T)$ is in a good correlation with $\Delta L/L(T)$; they have extremes in the similar temperature ranges (Figure 8a).

With the introduction of the large-sized La and Pr ions (Figures 8b and 9a), thermophysical properties do not undergo any significant changes over the entire investigated temperature range. This may be due to the small distortions of the unit cell in the PsC phase and the proximity of its configuration to the cubic syngony, and the change in the temperature only facilitates the transition to the purely cubic phase.

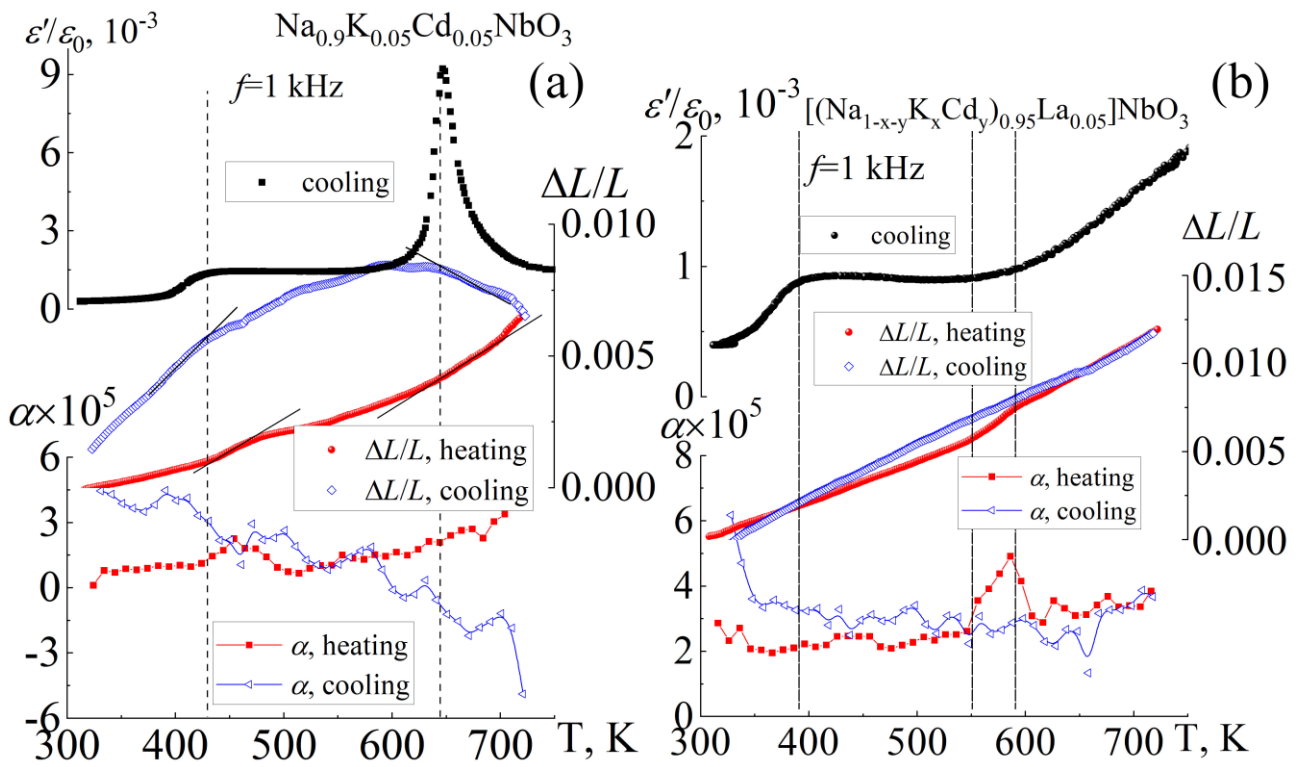


Figure 8. The dependence of ϵ''/ϵ_0 (upon cooling), α , and $\Delta L/L$ on the temperature of ceramic SSs: (a) $\text{Na}_{0.90}\text{K}_{0.05}\text{Cd}_{0.05}\text{NbO}_3$; (b) $[(\text{Na}_{0.90}\text{K}_{0.05}\text{Cd}_{0.05})_{0.95}\text{La}_{0.05}]\text{NbO}_3$.

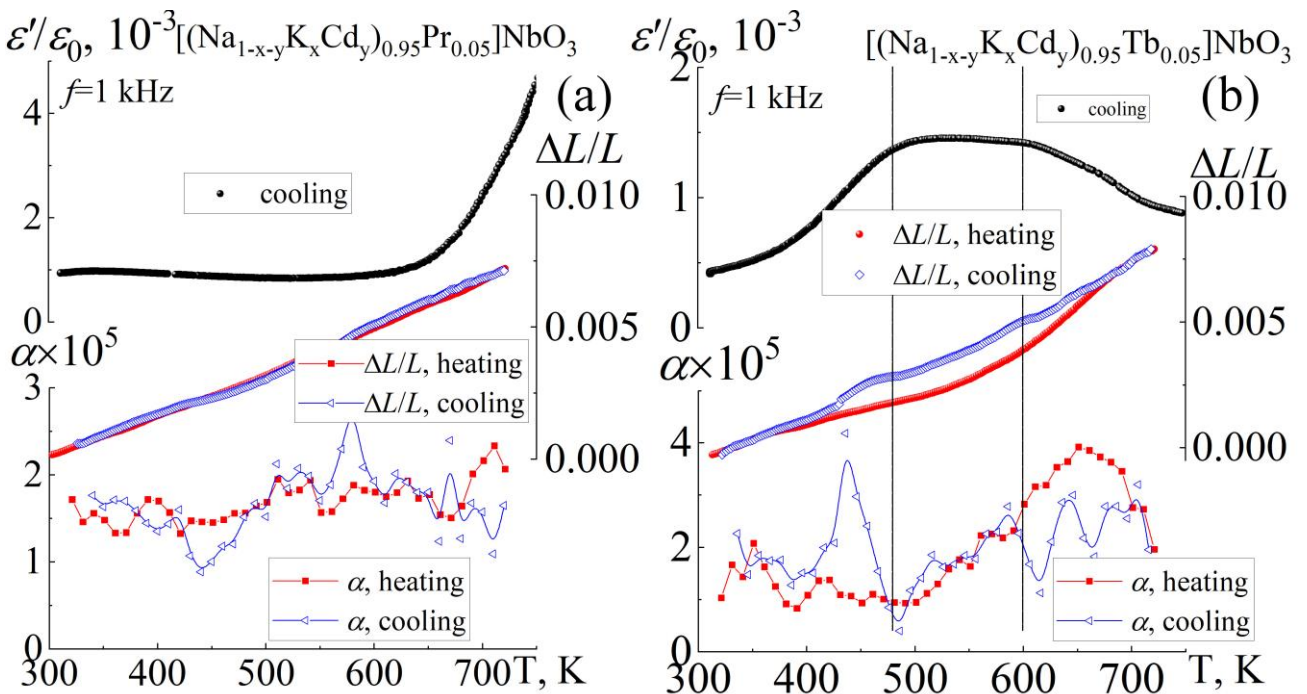


Figure 9. The dependence of ϵ''/ϵ_0 (upon cooling), α , and $\Delta L/L$ on the temperature of ceramic SSs: (a) $[(\text{Na}_{0.90}\text{K}_{0.05}\text{Cd}_{0.05})_{0.95}\text{Pr}_{0.05}]\text{NbO}_3$; (b) $[(\text{Na}_{0.90}\text{K}_{0.05}\text{Cd}_{0.05})_{0.95}\text{Tb}_{0.05}]\text{NbO}_3$.

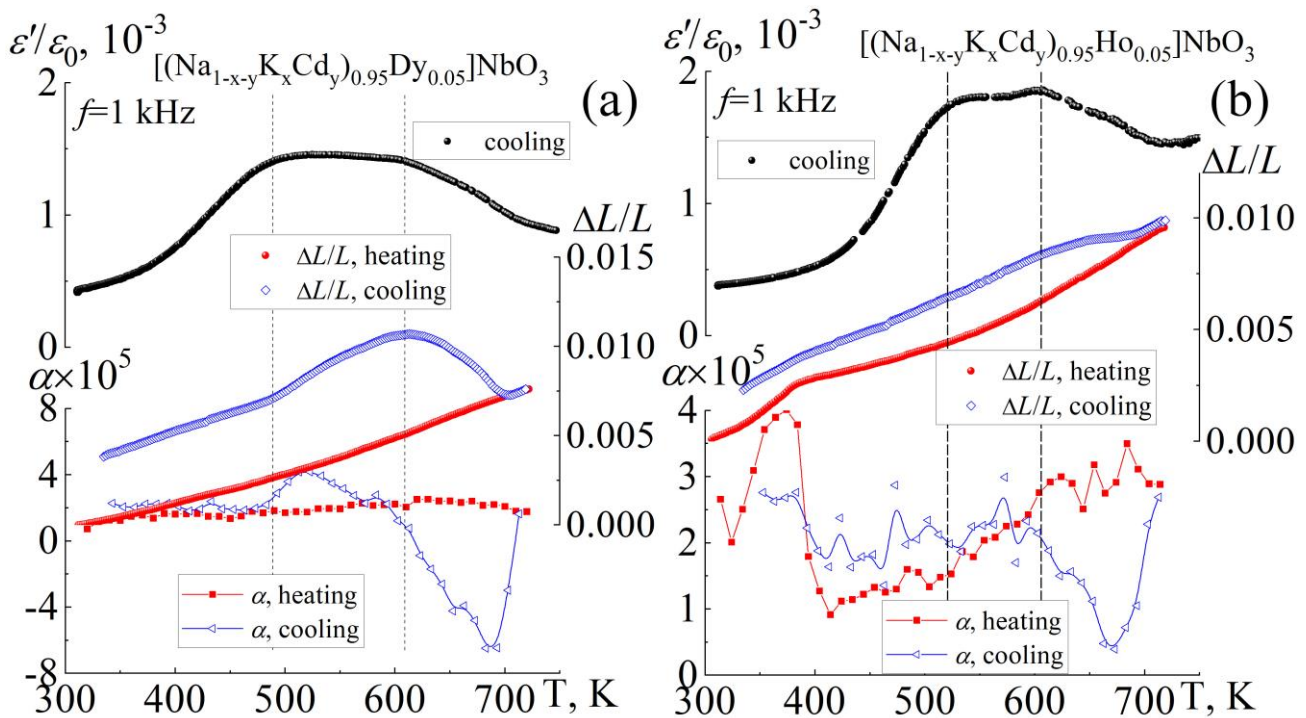


Figure 10. The dependence of ϵ'/ϵ_0 (upon cooling), α , and $\Delta L/L$ on the temperature of ceramic SSs: (a) $[(\text{Na}_{0.90}\text{K}_{0.05}\text{Cd}_{0.05})_{0.95}\text{Dy}_{0.05}]\text{NbO}_3$; (b) $[(\text{Na}_{0.90}\text{K}_{0.05}\text{Cd}_{0.05})_{0.95}\text{Ho}_{0.05}]\text{NbO}_3$.

For the SSs containing Tb, Dy, and Ho (Figures 9b and 10a,b), an almost monotonic increase in the $\Delta L/L$ dependence is characteristic with a change in the slope of the curves in the vicinity of the temperatures of the beginning and end of the plateau-like portion of the $\epsilon'/\epsilon_0(T)$ dependence. This occurs during cooling especially clearly in the SS with Dy (Figure 10a).

3.5. Microhardness

The results of studying the microhardness (H) of the ceramics by the comparative sclerometry method [52] and Young's modulus (E) determined from the load-displacement curves [53] are presented in Table 2. To reduce the standard error of the data, the microhardness values obtained at various loads, were averaged over several measurements. The results made it possible to estimate the stress intensity factor for mode I, K_{Ic} , which is a criterion for the crack resistance of the material. The crack resistance K_{Ic} was determined in accordance with the model of Anstis et al. [54,55] by the formula:

$$K_{Ic} = 0.016 \frac{E^{\frac{1}{2}} P}{H C^{\frac{3}{2}}}, \quad (4)$$

where P —applied load, E —Young's modulus, H —microhardness, and c —average distance from the center of the indentation to the end of the crack.

In general, all the considered UHP $[(\text{Na}_{0.90}\text{K}_{0.05}\text{Cd}_{0.05})_{0.95}\text{REE}_{0.05}]\text{NbO}_3$ ceramics have high hardness and Young's modulus and, as a consequence, good crack resistance for the ceramic materials (Table 2). However, the series contains samples of the SS modified with La and Pr; they have a pseudocubic structure, and their hardness is $H = 6.11 \pm 0.62$ GPa (La) and $H = 8.42 \pm 1.33$ GPa (Pr). Such a significant change in the microhardness of the ceramics is probably associated with a change in the symmetry of the perovskite cell and an increase in the syngony from monoclinic (lower category) to pseudocubic (higher category) for the $[(\text{Na}_{0.90}\text{K}_{0.05}\text{Cd}_{0.05})_{0.95}\text{La}_{0.05}]\text{NbO}_3$ and $[(\text{Na}_{0.90}\text{K}_{0.05}\text{Cd}_{0.05})_{0.95}\text{Pr}_{0.05}]\text{NbO}_3$ SS (Tables 1 and 2).

Table 2. The mechanical characteristics of the ceramic $\text{Na}_{0.90}\text{K}_{0.05}\text{Cd}_{0.05}\text{NbO}_3$ SS and the $[(\text{Na}_{0.90}\text{K}_{0.05}\text{Cd}_{0.05})_{0.95}\text{REE}_{0.05}]\text{NbO}_3$ SSs.

Composition	Young's Modulus, E , GPa	Microhardness, H , GPa	Crack Resistance, K_{Ic} , $\text{MPa m}^{0.5}$
$\text{Na}_{0.90}\text{K}_{0.05}\text{Cd}_{0.05}\text{NbO}_3$	297.8 ± 5.4	4.15 ± 0.49	2.34 ± 0.15
$[(\text{Na}_{0.90}\text{K}_{0.05}\text{Cd}_{0.05})_{0.95}\text{La}_{0.05}]\text{NbO}_3$	302.0 ± 3.2	6.11 ± 0.62	2.06 ± 0.2
$[(\text{Na}_{0.90}\text{K}_{0.05}\text{Cd}_{0.05})_{0.95}\text{Pr}_{0.05}]\text{NbO}_3$	347.3 ± 4.3	8.42 ± 1.33	2.2 ± 0.7
$[(\text{Na}_{0.90}\text{K}_{0.05}\text{Cd}_{0.05})_{0.95}\text{Tb}_{0.05}]\text{NbO}_3$	352.3 ± 5.9	4.47 ± 0.7	2.32 ± 0.35
$[(\text{Na}_{0.90}\text{K}_{0.05}\text{Cd}_{0.05})_{0.95}\text{Dy}_{0.05}]\text{NbO}_3$	369.9 ± 4.2	5.3 ± 0.96	2.02 ± 0.1
$[(\text{Na}_{0.90}\text{K}_{0.05}\text{Cd}_{0.05})_{0.95}\text{Ho}_{0.05}]\text{NbO}_3$	320.8 ± 5.5	4.85 ± 0.59	1.86 ± 0.2

3.6. Photoluminescence

The initial and modified with REE ceramics were transparent enough during UHP preparation (Figure 11). We decided to measure not only mechanical characteristics, but also optical (luminescent) characteristics of the pure and doped with 5 mol% of the REE (La, Pr, Tb, Dy, Ho) $\text{Na}_{0.90}\text{K}_{0.05}\text{Cd}_{0.05}\text{NbO}_3$ ceramics.

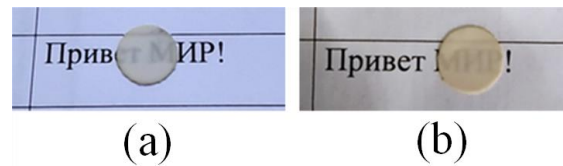


Figure 11. The samples of the translucent ceramics $[(\text{Na}_{0.90}\text{K}_{0.05}\text{Cd}_{0.05})_{0.95}\text{REE}_{0.05}]\text{NbO}_3$, obtained by UHP. Words mean “Hello, World!” (a) the pure sample, (b) the 5 mol% sample.

Figure 12 shows PL spectra of the pure and modified with the REE (La^{3+} , Pr^{3+} , Tb^{3+} , Dy^{3+} , Ho^{3+}) $\text{Na}_{0.90}\text{K}_{0.05}\text{Cd}_{0.05}\text{NbO}_3$ ceramic SSs. All PL spectra have two characteristic regions: from 380 to 575 nm and from 575 to 800 nm.

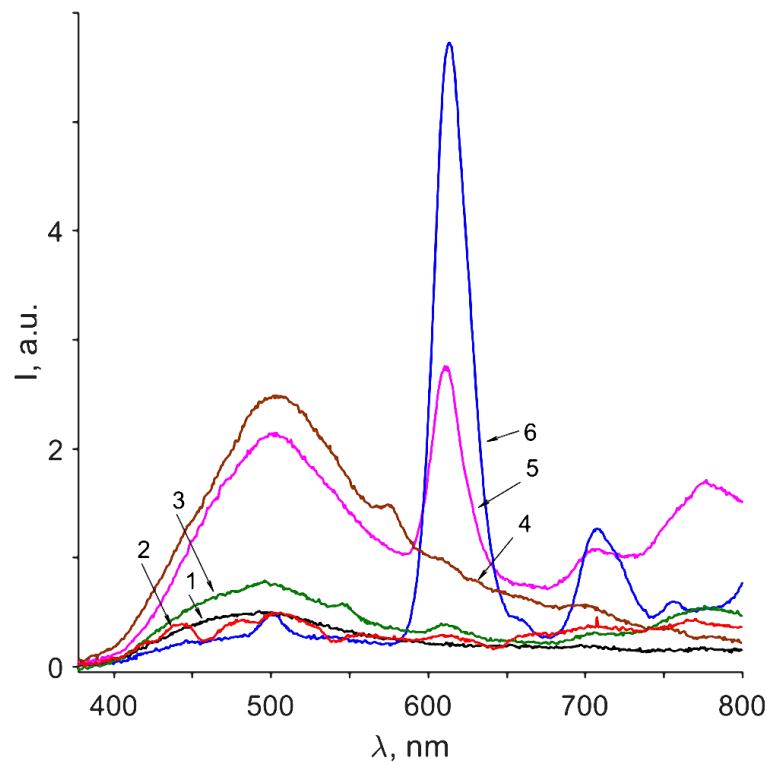


Figure 12. The PL spectra of the initial $\text{Na}_{0.90}\text{K}_{0.05}\text{Cd}_{0.05}\text{NbO}_3$ ceramics (1) and the modified ceramics: (2)—Ho, (3)—Tb, (4)—Dy, (5)—La, (6)—Pr. $T = 300\text{ K}$; $\lambda_{\text{ex}} = 325\text{ nm}$.

In the first region, a broad luminescent halo is observed with a maximum at about 500 nm. In the second region, several maxima of different intensities and widths are observed at ~610, 710, and 775 nm. In this case, the $[(\text{Na}_{0.90}\text{K}_{0.05}\text{Cd}_{0.05})_{0.95}\text{Pr}_{0.05}]\text{NbO}_3$ sample with a pseudocubic structure has the maximal PL.

In the unmodified $\text{Na}_{0.90}\text{K}_{0.05}\text{Cd}_{0.05}\text{NbO}_3$ ceramic sample, a very weak luminescent halo is observed with a maximum at ~500 nm (Figure 12 (curve 1)). This halo can be associated with the radiative recombination between the Nb^{5+} ion and the surrounding O^{2-} oxygen ions [56]. In addition, depending on the composition of the ceramics, the maximum of the luminescent halo for NaNbO_3 can shift from 480 to 540 nm, and the luminescence intensity decreases by half when the temperature changes from 90 to 50 K [57]. The KNbO_3 spectrum exhibits two luminescence maxima corresponding to its two polymorphic modifications: at 420 and 530 nm. In this case, the temperature quenching of the luminescence is observed at 70 and 30 K [57]. Thus, the low luminescence intensity of the $\text{Na}_{0.90}\text{K}_{0.05}\text{Cd}_{0.05}\text{NbO}_3$ ceramic matrix under normal conditions ($T = 300$ K) is apparently due to the presence of the temperature quenching of the radiative recombination of the Nb-O pair. In addition, it is possible that the energy transfers between different Nb-O pairs, surrounded by the metal cations with different ionic radii (Na, K, Cd—98, 133, 99 pm, respectively [58]), and then scatters on the vibrations of the crystal lattice.

Upon the modification of the $\text{Na}_{0.90}\text{K}_{0.05}\text{Cd}_{0.05}\text{NbO}_3$ SS with the REE, the shape of the spectrum changes and the intensity of the luminescence intensity distributes between the matrix itself and the characteristic intraconfigurational $4f^n-4f^n$ transitions of the REE (Figure 12 (2–6)).

Thus, the characteristic radiative transitions for Pr^{3+} ${}^3\text{P}_{0,1,2}-{}^3\text{H}_4$, ${}^1\text{D}_2-{}^3\text{H}_4$, and ${}^3\text{P}_0-{}^3\text{F}_2$ are located in the regions of 450–500, 620, and 660 nm, and the intensity of the maxima at 450–500 and 660 nm is minimal [59]. The typical radiative transitions for Dy^{3+} are ${}^4\text{F}_{9/2}-{}^6\text{H}_j$ ($J = 15/2, 13/2, \text{ and } 11/2$) at 476, 573, and 667 nm [60,61]; for Tb^{3+} ${}^5\text{D}_{3,4}-{}^7\text{F}_{4,5}$, and ${}^5\text{D}_4-{}^7\text{F}_j$ ($J = 6, 5, 4, \text{ and } 3$) at 442, 492, 548, 588, and 623 nm [61]; for Ho^{3+} ${}^5\text{F}_4-{}^5\text{I}_8$, ${}^5\text{S}_2-{}^5\text{I}_8$, and ${}^5\text{F}_5-{}^5\text{I}_8$ at 541, 551, and 653 nm [62].

The La^{3+} cation apparently lacks the $4f^n-4f^n$ transitions, since its electronic configuration is $4f^05d^16s^2$. Due to the fact that the excitation of the spectrum ($\lambda_{\text{ex}} = 325$ nm) is performed in the fundamental absorption region (3.41 eV for NaNbO_3 [63]), initially the spectrum of the ceramic matrix is excited; that is, the Nb-O pairs absorb and then radiate at 500 nm. Due to the charge transfer in the $\text{Pr}^{3+}-\text{Me}^{n+}$ ($\text{Me}^{n+} = \text{Ti}^{4+}, \text{Nb}^{5+}, \text{Ta}^{5+}, \text{ etc.}$) pair, the population of the ${}^1\text{D}_2$ state [63] is possible, from which the electrons pass into the basic ${}^3\text{H}_4$ state. In this case, the strong luminescence is observed in the region of ~610 nm, which is clearly seen in the spectrum of the $[(\text{Na}_{0.90}\text{K}_{0.05}\text{Cd}_{0.05})_{0.95}\text{Pr}_{0.05}]\text{NbO}_3$ ceramics (Figure 12 (6)). However, Figure 12 (2, 3) shows that there are no effective radiative recombination of the intraconfigurational $4f^n-4f^n$ transitions in the PL spectra of the $\text{Na}_{0.90}\text{K}_{0.05}\text{Cd}_{0.05}\text{NbO}_3$ samples modified with Tb^{3+} and Ho^{3+} .

This can be explained by the fact that during the synthesis of the ceramics, the valence of Tb can change from 3^+ to 4^+ , and with an increase in the annealing temperature to 1473 K, the number of Tb^{4+} ions also increases [59]. Such Tb^{4+} ions act as the quenching centers and not only reduce the amount of the Tb^{3+} ions, but also absorb the radiative recombination of the ${}^5\text{D}_{3,4}-{}^7\text{F}_j$ transitions [59]. Thus, it can be assumed that during the synthesis of the $[(\text{Na}_{0.90}\text{K}_{0.05}\text{Cd}_{0.05})_{0.95}\text{Tb}_{0.05}]\text{NbO}_3$ ceramics, the number of the Tb^{4+} cations increases, which acts as a luminescence quencher in the visible region. The Ho^{3+} ions are usually used as an activator in the up-conversion processes, where together with a sensitizer, usually the Yb^{3+} ions [64], the luminescence intensity is increased in the visible region excited by IR radiation. Thus, in the absence of a sensitizer, the probability of the radiative transitions in the visible region for Ho is small, and PL spectra of the $[(\text{Na}_{0.90}\text{K}_{0.05}\text{Cd}_{0.05})_{0.95}\text{Ho}_{0.05}]\text{NbO}_3$ ceramics prove it (Figure 12 (2)).

On the other hand, the Dy^{3+} ions in the $\text{Na}_{0.90}\text{K}_{0.05}\text{Cd}_{0.05}\text{NbO}_3$ matrix enhance the luminescence of the crystalline matrix. In this case, the PL intensity is five times higher

than in the unmodified ceramics (Figure 12 (1, 4)). Since the formation of the Dy^{2+} electron trap is possible only when exposed to the ionizing radiation, the luminescence of which is observed in the IR region at 1450 nm [65], the energy converses between the Dy^{3+} cations and the matrix. Moreover, the maximum luminescence intensity in the spectrum of $[(\text{Na}_{0.90}\text{K}_{0.05}\text{Cd}_{0.05})_{0.95}\text{Dy}_{0.05}]\text{NbO}_3$ ceramics is in the range of 480–540 nm (Figure 12 (4)). It should also be noted that an increase in the symmetry of the crystal structure of the samples under study can lead to an increase in the probability of the radiative transitions and energy transfer between the matrix and the REE cations in the visible wavelength range. This can be seen in the example of the $[(\text{Na}_{0.90}\text{K}_{0.05}\text{Cd}_{0.05})_{0.95}\text{Pr}_{0.05}]\text{NbO}_3$ and $[(\text{Na}_{0.90}\text{K}_{0.05}\text{Cd}_{0.05})_{0.95}\text{La}_{0.05}]\text{NbO}_3$ SSs, for which an increase in the symmetry of the structure leads to an increase in the luminescence intensity (Table 2 and Figure 8 (5, 6)).

4. Conclusions

Ceramic solid solutions (SSs) with the composition $\text{Na}_{0.90}\text{K}_{0.05}\text{Cd}_{0.05}\text{NbO}_3$ and $[(\text{Na}_{0.90}\text{K}_{0.05}\text{Cd}_{0.05})_{0.95}\text{REE}_{0.05}]\text{NbO}_3$ (where REE = La, Pr, Tb, Dy, Ho) were synthesized for the first time by uniaxial hot pressing (UHP). XRD analysis showed changes in the structural characteristics of the SS $\text{Na}_{0.90}\text{K}_{0.05}\text{Cd}_{0.05}\text{NbO}_3$ upon its modification with REEs La, Pr, Tb, Dy, and Ho. XRD also proved the absence of impurities. The volume of the perovskite unit cell slightly increases upon the introduction of large-size ions La^{3+} and Pr^{3+} , which indicates their incorporation into the crystal lattice of the initial solid solution. It was shown that the REEs Tb, Dy, and Ho do not completely enter the crystal lattice of the initial solid solution, but form impurity compounds LnNbO_4 of the monoclinic fergusonite type.

It was found that UHP ceramics have a homogeneous fine-grained structure with increased mechanical characteristics: hardness, Young's modulus, and high crack resistance.

A study of the dielectric and thermophysical properties in a wide temperature range revealed the formation in the initial solid solution $\text{Na}_{0.90}\text{K}_{0.05}\text{Cd}_{0.05}\text{NbO}_3$ of two peaks of the dielectric constant. They correspond to the transition from orthorhombic to tetragonal (T_{O-T}) and from tetragonal to cubic (T_{T-C}) phase. The introduction of large-sized REEs shifted T_{O-T} and T_{T-C} to the low-temperature region. However, introduction of middle- and small-sized REEs shifts $T \rightarrow C$ transition to a low-temperature and $O \rightarrow T$ transition to a high-temperature region; they merge and form a quasi-plateau region. This may be caused by the different incorporation mechanisms of REEs to the crystal lattice of investigated SSs.

The dispersion of the permittivity is observed in the paraelectric region of both original and modified SSs. This may be due to the redox processes that exist due to the variable valence of niobium. Redox processes cause the appearance of oxygen vacancies, and as a result, increase electrical conductivity and its contribution to the permittivity.

Both the real and imaginary parts of the relative permittivity are blurred with the introduction to SS of all studied modifiers. The greatest influence is exerted by medium- and small-sized REE. This might be explained by the following: they partially incorporate into the structure and form non-ferroelectric ballast phases.

Anomalies of thermophysical characteristics correspond to the above-described changes in dielectric properties in the entire studied temperature range: in the vicinity of phase transitions, the thermophysical characteristics are extreme. The thermophysical characteristics experience changes in those intervals where the dielectric properties do not exhibit anomalous behavior. This indicates the existence of small structural instabilities. However, confirmation requires additional XRD studies.

Very weak luminescence intensity from the electron-hole pair $\text{Nb}^{4+}-\text{O}^-$ was observed in the green region with a maximum at ~ 500 nm for the ceramic SS $\text{Na}_{0.90}\text{K}_{0.05}\text{Cd}_{0.05}\text{NbO}_3$. At the same time, in the $\text{Na}_{0.90}\text{K}_{0.05}\text{Cd}_{0.05}\text{NbO}_3$ SS and SSs modified with Ho and Tb a low intense luminescence of the ceramic matrix is observed in comparison with the intensity of luminescence of the matrix in the $\text{Na}_{0.90}\text{K}_{0.05}\text{Cd}_{0.05}\text{NbO}_3$ samples modified with La and Dy. The intensity is low due to the energy dissipation on the crystal lattice vibrations and the influence of the REE cations on the charge transfer between different

NbO groups. Thus, the modification by Tb and Ho does not lead to an increase in the luminescence of the $\text{Na}_{0.90}\text{K}_{0.05}\text{Cd}_{0.05}\text{NbO}_3$ ceramics in the visible region, in contrast to the modification by Dy^{3+} . In the modification by Dy^{3+} case the luminescence intensity in the visible region increases by a factor of five. An increase in the symmetry of the $[(\text{Na}_{0.90}\text{K}_{0.05}\text{Cd}_{0.05})_{0.95}\text{La}(\text{Pr})_{0.05}]\text{NbO}_3$ SS leads to a more efficient radiative recombination between Nb-O. This is apparently due to the efficient transfer of the energy between the matrix and REE, which, in particular, leads to very intense luminescence due to the radiative $^1\text{D}_2\text{-}^3\text{H}_4$ transition of the Pr^{3+} ion in the $[(\text{Na}_{0.90}\text{K}_{0.05}\text{Cd}_{0.05})_{0.95}\text{Pr}^{3+}_{0.05}]\text{NbO}_3$ ceramics near ~610 nm. The study of optical characteristics of $[(\text{Na}_{0.90}\text{K}_{0.05}\text{Cd}_{0.05})_{0.95}\text{REE}_{0.05}]\text{NbO}_3$ Ss synthesized in this study widens their potential application as luminescent materials.

Author Contributions: A.K.: Conceptualization, Methodology, Investigation, Supervision, Writing—Original Draft, Visualization, Investigation, Validation, Methodology, Data Curation. M.P.: Conceptualization, Writing—Original Draft. L.S.: Investigation, Writing—Review and Editing. A.N.: Investigation, Visualization. O.S.: Conceptualization, Writing—Original Draft, Writing—Review and Editing, Visualization, Investigation, Validation, Methodology, Data Curation. M.S.: Writing—Original Draft, Investigation, Validation, Methodology, Data Curation. N.S.: Writing—Original Draft, Investigation, Validation. S.K.: Investigation, Validation, Writing—Review and Editing. A.R.: Visualization, Data Curation, Validation. D.R.: Investigation, Visualization. L.R.: Conceptualization, Writing—Original Draft, Supervision, Writing—Review and Editing. All authors have read and agreed to the published version of the manuscript.

Funding: The study was carried out with the financial support of the Ministry of Science and Higher Education of the Russian Federation, topic FENW-2023-0010.

Institutional Review Board Statement: Not applicable.

Informed Consent Statement: Not applicable.

Data Availability Statement: The raw data required to reproduce these findings are available from the corresponding author on a reasonable request.

Acknowledgments: The equipment of the Center of Research Institute of Physics SFedU, “High-Tech” SFedU was used in this study. We thank the center for the given opportunity.

Conflicts of Interest: The authors declare no conflict of interest. The funders had no role in the design of the study; in the collection, analyses, or interpretation of data; in the writing of the manuscript; or in the decision to publish the results.

References

1. Von Hippel, A. Ferroelectricity, domain structure, and phase transitions of barium titanate. *Rev. Modern Phys.* **1950**, *22*, 221–237. [[CrossRef](#)]
2. Merz, W.J. Domain properties in BaTiO_3 . *Phys. Rev.* **1952**, *88*, 421–422. [[CrossRef](#)]
3. Landauer, R. Electrostatic considerations in BaTiO_3 domain formation during polarization reversal. *J. Appl. Phys.* **1957**, *28*, 227–234. [[CrossRef](#)]
4. Last, J.T. Infrared-absorption studies on barium titanate and related materials. *Phys. Rev.* **1957**, *105*, 1740–1750. [[CrossRef](#)]
5. Wentz, J.L.; Kennedy, L.Z. Primary pyroelectric effect in the PZT 95/5 ceramic. *J. Appl. Phys.* **1964**, *35*, 1767–1770. [[CrossRef](#)]
6. Linde, R.K. Depolarization of ferroelectrics at high strain rates. *J. Appl. Phys.* **1967**, *38*, 4839–4842. [[CrossRef](#)]
7. Carruthers, J.R.; Grasso, M. Phase equilibria relations in the ternary system $\text{BaO-SrO-Nb}_2\text{O}_5$. *J. Electrochem. Soc.* **1970**, *117*, 1426. [[CrossRef](#)]
8. Itoh, Y.; Lwasaki, H. Tungsten bronze field in the pseudo-ternary system $\text{NaNbO}_5\text{-BaTiO}_3\text{-BaNb}_2\text{O}_6$. *Mat. Res. Bull.* **1972**, *7*, 663–672. [[CrossRef](#)]
9. Ogawa, T.; Wakino, K. The temperature property of frequency constant of $\text{Pb}(\text{Sn}_{1/2}\text{Sb}_{1/2})\text{O}_3\text{-PbTiO}_3\text{-PbZrO}_3$ piezoelectric ceramics. *J. Jpn. Soc. Powder Powder Metall.* **1977**, *24*, 123–127. [[CrossRef](#)]
10. Gonnard, P.; Troccaz, M. Dopant Distribution between A and B Sites in the PZT Ceramics of Type ABO_3 . *J. Sol. St. Chem.* **1978**, *23*, 321–326. [[CrossRef](#)]
11. Tsubouchi, N.; Takahashi, M.; Chino, T.; Akashi, T.; Tokyo-to, Japan, Tokyo, Assignors to Nippon Electric Company, Limited. Piezoelectric Ceramic. US Patent No. 3595795, 1971.
12. Nippon Electric Company, Limited, Tokyo, Japan. Piezoelectric Ceramic Material. France Patent No. FR1580831A, 28 December 1969.

13. Murty, S.N.; Ramana, K.V.M.; Umakantham, K.; Bhanumathi, A. Modified (NaK)NbO₃ ceramics for transducer applications. *Ferroelectrics* **1990**, *102*, 243–247. [[CrossRef](#)]
14. Murty, S.N. Piezoelectric (NaK)NbO₃ ceramics for ultrasonic delay line applications. *Ferroelectrics* **1994**, *154*, 171–176. [[CrossRef](#)]
15. Shan, Y.; Sinozaki, N.; Nakamura, T. Preparation and characterizations of new perovskite oxides (La_xNa_{1–3x–y}Li_y□_{2x})NbO₃ (0.0 ≤ x and y ≤ 0.2). *Sol. St. Ion.* **1998**, *108*, 403–406. [[CrossRef](#)]
16. Wang, X.; Helmersson, U.; Olafsson, S.; Rudner, S.; Wernlund, L.D.; Gevorgian, S. Growth and field dependent dielectric properties of epitaxial Na_{0.5}K_{0.5}NbO₃ thin films. *Appl. Phys. Lett.* **1998**, *73*, 927–929. [[CrossRef](#)]
17. EU. Commission Directive 2013/28/EU of 17 May 2013 amending annex II to directive 2000/53/EC of the European Parliament and of the Council on end-of-life vehicles. *Off. J. Eur. Union* **2013**, *L135*, 14–18.
18. Zhang, S.T.; Kounga, A.B.; Aulbach, E.; Ehrenberg, H.; Rödel, J. Giant strain in lead-free piezoceramics Bi_{0.5}Na_{0.5}TiO₃-BaTiO₃-K_{0.5}Na_{0.5}NbO₃ system. *Appl. Phys. Lett.* **2007**, *91*, 2–5. [[CrossRef](#)]
19. Rödel, J.; Jo, W.; Seifert, K.T.P.; Anton, E.M.; Granzow, T.; Damjanovic, D. Perspective on the development of lead-free piezoceramics. *J. Amer. Ceram. Soc.* **2009**, *92*, 1153–1177. [[CrossRef](#)]
20. Matsubara, M.; Yamaguchi, T.; Wataru, S.; Koichi, K.; Yogo, T.; Hirano, S. Processing and Piezoelectric Properties of Lead-Free (K, Na)(Nb, Ta)O₃ Ceramics. *J. Am. Ceram. Soc.* **2005**, *88*, 1190–1196. [[CrossRef](#)]
21. Verbenko, I.A.; Razumovskaya, O.N.; Shilkina, L.A.; Reznichenko, L.A.; Andryushin, K.P. Production and dielectric properties of lead-free ceramics with the formula [(Na_{0.5}K_{0.5})_{1–x}Li_x](Nb_{1–y–z}Ta_ySb_z)O₃. *Inorg. Mater.* **2009**, *45*, 702–708. [[CrossRef](#)]
22. Saito, Y.; Takao, H.; Tani, T.; Nonoyama, T.; Takatori, K.; Homma, T.; Nagaya, T.; Nakamura, M. Lead-free piezoceramics. *Nature* **2004**, *432*, 84–87. [[CrossRef](#)]
23. Li, P.; Zhai, J.; Shen, B.; Zhang, S.; Li, X.; Zhu, F.; Zhang, X. Ultrahigh piezoelectric properties in textured (K, Na)NbO₃-based lead-free ceramics. *Adv. Mater.* **2018**, *30*, 1705171. [[CrossRef](#)]
24. Wu, J.; Xiao, D.; Zhu, J. Potassium-sodium niobate lead-free piezoelectric materials: Past, present, and future of phase boundaries. *Chem. Rev.* **2015**, *115*, 2559–2595. [[CrossRef](#)]
25. Jo, W.; Dittmer, R.; Acosta, M.; Zang, J.; Groh, C.; Sapper, E.; Wang, K.; Rödel, J. Giant electric-field-induced strains in lead-free ceramics for actuator applications—Status and perspective. *J. Electroceram.* **2012**, *29*, 71–93. [[CrossRef](#)]
26. Li, W.; Hao, J.; Li, W.; Du, J.; Fu, P.; Sun, W.; Chen, C.; Xu, Z.; Chu, R. Electrical properties and luminescence properties of 0.96(K_{0.48}Na_{0.52})(Nb_{0.95}Sb_{0.05})–0.04Bi_{0.5}(Na_{0.82}K_{0.18})_{0.5}ZrO₃-xSm lead-free ceramics. *J. Adv. Ceram.* **2020**, *9*, 72–82. [[CrossRef](#)]
27. Andryushin, K.P.; Shilkina, L.A.; Andryushina, I.N.; Moysa, M.O.; Rudsky, D.I.; Reznichenko, L.A. Crystal structure, polarization properties and reverse nonlinearity of solid solutions of the KNN-PZT system in a wide range of external influences. *Ceram. Intern.* **2021**, *47*, 138–148. [[CrossRef](#)]
28. Nagaenko, A.V.; Chang, S.H.; Andryushin, K.P.; Shilkina, L.A.; Mazuritskiy, M.I.; Andryushina, I.N.; Glazunova, E.V.; Pavelko, A.A.; Trusov, Y.A.; Verbenko, I.A.; et al. Multi-element ferroactive materials based on KNN-PZT compositions with fundamentally different physical properties. *Heliyon* **2020**, *6*, e03497. [[CrossRef](#)] [[PubMed](#)]
29. Rödel, J.; Webber, K.G.; Dittmer, R.; Jo, W.; Kimura, M.; Damjanovic, D. Transferring lead-free piezoelectric ceramics into application. *J. Europ. Ceram. Soc.* **2015**, *35*, 1659–1681. [[CrossRef](#)]
30. Andryushin, K.; Shilkina, L.; Andryushina, I.; Nagaenko, A.; Moysa, M.; Dudkina, S.; Reznichenko, L. Features of the Structure and Electrophysical Properties of Solid Solutions of the System (1-x-y) NaNbO₃-xKNbO₃-yCd_{0.5}NbO₃. *Materials* **2021**, *14*, 4009. [[CrossRef](#)]
31. Isupov, V.A. Physical phenomena in ferroelectric complex perovskites. *Bull. Acad. Sci. U.S.S.R. Phys. Ser.* **1982**, *47*, 136–141.
32. Von der Mühl, R.; Sadel, A.; Hagenmuller, P. Structure cristalline a 295 K de la phase ferroelectrique Li_{0,02}Na_{0,98}NbO₃. *J. Sol. St. Chem.* **1984**, *51*, 176–182. [[CrossRef](#)]
33. Isupov, V.A. Crumbling -type phase transitions. *Cryst. Rep.* **1959**, *4*, 603–608. (In Russian)
34. Megaw, H.D. The Seven Phases of Sodium Niobate. *Ferroelectrics* **1974**, *7*, 87–89. [[CrossRef](#)]
35. Chen, J.; Feng, D. In situ TEM studies of para-ferro phase transitions in NaNbO₃. *Phys. Stat. Sol. A* **1988**, *109*, 427–434. [[CrossRef](#)]
36. Reznichenko, L.A.; Shilkina, L.A. Morphotropic Phase in the NaNbO₃-LiNbO₃ Solid-Solution System. *Bull. Acad. Sci. U.S.S.R. Phys. Ser.* **1975**, *39*, 1118–1121.
37. Reznichenko, L.A.; Shilkina, L.A.; Razumovskaya, O.N.; Dudkina, S.I.; Gagarina, E.S.; Borodin, A.V. Dielectric and piezoelectric properties of NaNbO₃-based solid solutions. *Inorg. Mater.* **2003**, *39*, 139–151. [[CrossRef](#)]
38. Fesenko, E.G. *The Perovskite Family and Ferroelectricity*; (In Russian: Semejstvo Perovskita I Segnetoelektrichestvo); Atomizdat: Moscow, Russia, 1972.
39. JCPDS. *Powder Diffraction File*; Data Card. Inorganic Section. Set, card; JCPDS: Swarthmore, PA, USA, 1948.
40. Urusov, V.S. *Theory of Isomorphic Miscibility*; Science: Moscow, Russia, 1977; (In Russian: Teoriya izomorfnoy smesimosti).
41. Dantsiger, A.Y.; Reznichenko, L.A.; Dudkina, S.I.; Razumovskaya, O.N.; Shilkina, L.A. Correlation between the microstructure of ferroelectric ceramics and their chemical and phase composition, the degree of perfection of the crystal structure and the preparation conditions. *Ferroelectrics* **1998**, *214*, 255–259. [[CrossRef](#)]
42. Rao, C.N.R.; Gopalakrishnan, J. *New Directions in Solid State Chemistry*; Cambridge University Press: Cambridge, UK, 1986.
43. Hedvall, J.A. Über die physikalisch-chemischen Prozesse beim Zusammenbacken von angeschmolzenen Pulvern. *Z. Phys. Chem.* **1926**, *123U*, 33–85. [[CrossRef](#)]

44. Liu, L.; Huang, Y.; Li, Y.; Fang, L.; Dammak, H.; Fan, H.; Thi, M.P. Orthorhombic to tetragonal structural phase transition in $\text{Na}_{0.5}\text{K}_{0.5}\text{NbO}_3$ -based ceramics. *Mater. Lett.* **2012**, *68*, 300–302. [[CrossRef](#)]
45. Du, H.; Huang, Y.H.; Tang, H.; Qin, H.; Feng, W. Dielectric and piezoelectric properties of SrZrO_3 -modified $(\text{K}_{0.45}\text{Na}_{0.51}\text{Li}_{0.04})(\text{Nb}_{0.90}\text{Ta}_{0.04}\text{Sb}_{0.06})\text{O}_3$ lead-free piezoceramics. *Mater. Lett.* **2013**, *106*, 141–144. [[CrossRef](#)]
46. Shi, W.; Feng, Y.; Lu, T.; Lu, Y.; Shen, J.; Xue, J.; Du, J.; Fu, P.; Hao, J.; Li, W. Photoluminescence and impedance properties of rare-earth doped $(\text{K}_{0.5}\text{Na}_{0.5})\text{NbO}_3$ lead-free ceramics. *J. Mater. Sci. Mater. Electron.* **2019**, *30*, 9–16. [[CrossRef](#)]
47. Egerton, L.; Dillon, D.M. Piezoelectric and Dielectric Properties of Ceramics in the System Potassium—Sodium Niobate. *J. Amer. Ceram. Soc.* **1959**, *42*, 438–442. [[CrossRef](#)]
48. Zhang, N.; Lv, X.; Zhang, X.-X.; Lyu, X.; Yang, S.-W.; Wu, J. Low-temperature dielectric relaxation associated with NbO_6 octahedron distortion in antimony modified potassium sodium niobate ceramics. *J. Mater. Sci. Technol.* **2022**, *115*, 189–198. [[CrossRef](#)]
49. Uchino, K.; Nomura, S. Critical exponents of the dielectric constants in diffused-phase-transition crystals. *Ferroelectrics* **1982**, *44*, 55–61. [[CrossRef](#)]
50. Liu, L.; Knapp, M.; Ehrenberg, H.; Fang, L.A.; Fan, H.; Schmitt, L.; Fuess, H.; Hoelzel, M.; Dammak, H.; Thi, M.P.; et al. Average vs. local structure and composition-property phase diagram of $\text{K}_{0.5}\text{Na}_{0.5}\text{NbO}_3\text{-Bi}_{\frac{1}{2}}\text{Na}_{\frac{1}{2}}\text{TiO}_3$ system. *J. Europ. Ceram. Soc.* **2017**, *37*, 1387–1399. [[CrossRef](#)]
51. Zhai, Y.; Du, J.; Chen, C.; Hao, J.; Fu, P.; Li, W.; Xu, Z. Temperature stability and electrical properties of Tm_2O_3 doped KNN-based ceramics. *J. Mater. Sci. Mater. Electron.* **2019**, *30*, 4716–4725. [[CrossRef](#)]
52. Oliver, W.; Pharr, G.M. Measurement of hardness and elastic modulus by instrumented indentation: Advances in understanding and refinements to methodology. *J. Mater. Res.* **2004**, *19*, 3. [[CrossRef](#)]
53. Maslennikov, I.I.; Reshetov, V.N.; Useinov, A.S. Mapping the elastic modulus of a surface with a NanoScan 3D scanning microscope. *Instrum. Experim. Tech.* **2015**, *58*, 711–717. [[CrossRef](#)]
54. Anstis, G.R.; Chantikul, P.; Lawn, B.R.; Marshall, D. A Critical Evaluation of Indentation Techniques for Measuring Fracture Toughness: I, Direct Crack Measurements. *Transformation* **1981**, *46*, 533–538. [[CrossRef](#)]
55. Chantikul, P.; Anstis, G.R.; Lawn, B.R.; Marshall, D. A Critical Evaluation of Indentation Techniques for Measuring Fracture Toughness: II, Strength Method. *J. Amer. Ceram. Soc.* **1981**, *64*, 539–543. [[CrossRef](#)]
56. Blasse, G.; Brill, A. Luminescence phenomena in compounds with fergusonite structure. *J. Luminesc.* **1970**, *3*, 109–131. [[CrossRef](#)]
57. Blasse, G.; De Haart, L. The nature of the luminescence of niobates MNbO_3 ($M = \text{Li, Na, K}$). *Mater. Chem. Phys.* **1986**, *14*, 481–484. [[CrossRef](#)]
58. Shaskolskaya, M.P. *Crystallography: Textbook. Manual for Technical Colleges*, 2nd ed.; Higher School: Moscow, Russia, 1984; (In Russian: Kristallografiya: Ucheb. posobiye dlya vtuzov. -2-ye izd., pererab. i dop.).
59. Verma, R.K.; Kumar, K.; Rai, S. Inter-conversion of Tb^{3+} and Tb^{4+} states and its fluorescence properties in $\text{MO-Al}_2\text{O}_3$: Tb ($M = \text{Mg, Ca, Sr, Ba}$) phosphor materials. *Sol. St. Sci.* **2010**, *12*, 1146–1151. [[CrossRef](#)]
60. Wen, R.; Zhou, L.; Zou, X.; Luo, L.; Jiang, N.; Zheng, Q.; Liao, J.; Xu, C.; Lin, D. Phase transition, electrical and luminescent properties of Dy-doped $\text{K}_{0.5}\text{Na}_{0.5}\text{NbO}_3$ -based lead-free ceramics. *J. Mater. Sci. Mater. Electron.* **2015**, *26*, 8341–8349. [[CrossRef](#)]
61. Ramachari, D.; Moorthy, L.R.; Jayasankar, C.K. Energy transfer and photoluminescence properties of $\text{Dy}^{3+}/\text{Tb}^{3+}$ co-doped oxyfluorosilicate glass-ceramics for solid-state white lighting. *Ceram. Intern.* **2014**, *40*, 11115–11121. [[CrossRef](#)]
62. Zhang, Y.; Liu, J.; Sun, H.; Peng, D.; Li, R.; Bulin, C.; Wang, X.; Zhang, Q.; Hao, X. Reversible luminescence modulation of Ho-doped $\text{K}_{0.5}\text{Na}_{0.5}\text{NbO}_3$ piezoelectrics with high luminescence contrast. *J. Am. Ceram. Soc.* **2018**, *101*, 2305–2312. [[CrossRef](#)]
63. Yang, X.; Zhao, L.; Chen, W.; Liu, Z.; Fan, X.; Tian, S.; Xu, X.; Qiu, J.; Yu, X. Low-temperature red long-persistent luminescence of Pr^{3+} doped NaNbO_3 with a perovskite structure. *J. Luminesc.* **2019**, *208*, 290–295. [[CrossRef](#)]
64. Kir'yanov, A.V.; Aboites, V.; Belovolov, A.M.; Damzen, M.; Minassian, A.; Timoshechkin, M.; Belovolov, M. Visible-to-near-IR luminescence at stepwise up-conversion in Yb, Ho: GGG under IR diode pumping. *J. Luminesc.* **2003**, *102–103*, 715–721. [[CrossRef](#)]
65. Schuyt, J.J.; Williams, G.V.M. Photoluminescence of Dy^{3+} and Dy^{2+} in NaMgF_3 :Dy: A potential infrared radiophotoluminescence dosimeter. *Radiat. Meas.* **2020**, *134*, 106326. [[CrossRef](#)]

Disclaimer/Publisher's Note: The statements, opinions and data contained in all publications are solely those of the individual author(s) and contributor(s) and not of MDPI and/or the editor(s). MDPI and/or the editor(s) disclaim responsibility for any injury to people or property resulting from any ideas, methods, instructions or products referred to in the content.